Input-adaptive linear mixed-effects model for estimating alveolar Lung Deposited Surface Area (LDSA) using multipollutant datasets

Pak Lun Fung[1,2], Martha A. Zaidan[1,2,3], Jarkko V. Niemi[4], Erkka Saukko[5], Hilkka Timonen[6], Anu Kousa[4], Joel Kuula[6], Topi Rönkkö[7], Ari Karppinen[6], Sasu Tarkoma[8], Markku Kulmala[1,3], Tuukka Petäjä[1,3] and Tareq Hussein[1,9]

[1]Institute for Atmospheric and Earth System Research / Physics, Faculty of Science, University of Helsinki, Finland
[2]Helsinki Institute of Sustainability Science, Faculty of Science, University of Helsinki, Finland
[3]Joint International Research Laboratory of Atmospheric and Earth System Sciences, School of Atmospheric Sciences, Nanjing University, Nanjing 210023, China
[4]Helsinki Region Environmental Services Authority (HSY), P.O. Box 100, FI-00066 Helsinki, Finland
[5]Pegasor Ltd., FI-33100 Tampere, Finland
[6]Atmospheric Composition Research, Finnish Meteorological Institute, FI-00560 Helsinki, Finland
[7]Aerosol Physics Laboratory, Physics Unit, Tampere University, FI-33720 Tampere, Finland
[8]Department of Computer Science, Faculty of Science, University of Helsinki, Finland
[9]Department of Physics, the University of Jordan, Amman 11942, Jordan

Correspondence to: Pak Lun Fung (pak.fung@helsinki.fi), Tareq Hussein (tareq.hussein@helsinki.fi)

Abstract. Lung deposited surface area (LDSA) has been considered to be a better metric to explain nanoparticle toxicity instead of the commonly used particulate mass concentration. LDSA concentrations can be obtained either by direct measurements or by calculation based on the empirical lung deposition model and measurements of particle size distribution. However, the LDSA or size distribution measurements are neither compulsory nor regulated by the government. As a result, LDSA data are often scarce spatially and temporally. In light of this, we develop a novel statistical model, named input-adaptive mixed-effects (IAME) model, to estimate LDSA based on other already existing measurements of air pollutant variables and meteorological conditions. During the measurement period in 2017–2018, we retrieved LDSA data measured by Pegasor AQ Urban and other variables at a street canyon (SC, average LDSA = 19.7±11.3 µm^2 cm^{-3}) site and an urban background (UB, average LDSA = 11.2±7.1 µm^2 cm^{-3}) site in Helsinki, Finland. For the continuous estimation of LDSA, the IAME model was automatised to select the best combination of input variables, including a maximum of three fixed effect variables and three time indictors as random effect variables. Altogether, 696 sub-models were generated and ranked by the coefficient of determination (R^2), mean absolute error (MAE) and centred root-mean-square differences ($cRMSD$) in order. At the SC site, the LDSA concentrations were best estimated by mass concentration of particle of diameters smaller than 2.5 µm (PM$_{2.5}$), total particle number concentration (PNC) and black carbon (BC), all of which are closely connected with the vehicular emissions. At the UB site the LDSA concentrations were found to be correlated with PM$_{2.5}$, BC and carbon monoxide (CO). The accuracy of the overall model was better at the SC site (R^2 = 0.80, MAE = 3.7 µm^2 cm^{-3}) than at the UB site (R^2 = 0.77, MAE = 2.3 µm^2 cm^{-3}) plausibly because the LDSA source was more tightly controlled by the close-by vehicular emission source. The results also demonstrated that the additional adjustment by taking random effects into account improved the sensitivity and the accuracy of the fixed effect model. Due to its adaptive input selection and inclusion of random effects, IAME could fill up missing data or even serve as a network of virtual sensors to complement the measurements at reference stations.

1 Introduction

Particulate matter is one of the key components determining urban air pollution. Particulate matter can be described by a combination of varying concentration (number, surface area and mass) and chemical composition. The mass concentrations of particulate matter are dominated by large particles whereas the number concentrations are governed by sub-micron particles (particle diameter (d$_p$) <1 µm), particularly ultrafine particles (UFP, d$_p$< 0.1 µm) (e.g. Petäjä et al., 2007; Rönkkö et al., 2017;

43 Zhou et al., 2020). Particulate matter of varying sizes, carrying various harmful substances, have been known for playing a

44 major role in adverse health effects (Dockery et al., 1993; Oberdorster, 2012; Shiraiwa et al., 2017) in particular to respiratory

45 systems. A particle could be deposited in lung airways upon inhalation (Oberdörster et al., 2005) through three main

46 mechanisms: inertial impaction, gravitational sedimentation and Brownian diffusion. An airborne particle might be inhaled

47 either through nasal or oral passage and enter the respiratory tract. Coarser particles are usually partly deposited in the head

48 airway by the inertial impaction mechanism because they cannot follow the air streamline. Some finer particles are deposited

49 in the tracheobronchial region, mainly through gravitational sedimentation while some are removed by mucociliary clearance

50 (Gupta and Xie, 2018). The remaining sub-micron particles diffuse by Brownian motion and penetrate deeply into the alveolar

51 region, which is considered to be the most vulnerable section in lungs because removal mechanisms might be insufficient

52 (Gupta and Xie, 2018). The surface area of inhaled particulate matter could also act as a transport vector for many bacteria and

53 viruses (Liu et al., 2018a), and therefore, besides commonly monitored particulate matter number concentration and mass

54 concentration, the surface area of a particle is also an important factor when considering the harmfulness of particulate matter

55 (Duffin et al., 2002). In particular, the total surface area of particles which are deposited in alveolar section of human lungs,

56 known as Lung Deposited Surface Area (LDSA), is of the greatest concern because in vitro nanoparticle toxicity has been

57 demonstrated to be better explained when the lung burden was expressed as total particle surface area instead of atmospheric

58 particulate matter mass (e.g. Brown et al., 2001; Oberdorster, 2012; Schmid and Stoeger, 2016).

59

60 LDSA can be considered as an intermediary parameter between particle mass and particle number concentration as it cannot

61 be simply inferred from either of those parameters. Moreover, due to the various deposition efficiency with respect to particle

62 sizes, the quantification of LDSA is not simple. Conventionally, LDSA concentrations can be retrieved by (1) derivation from

63 particle size distribution with a deposition model or (2) direct measurements.

64

65 By fitting experimental lung deposition data on human beings, empirical deposition models are developed with the use of the

66 lung deposition model modified by Yeh and Schum (1980). Examples include the International Commission on Radiological

67 Protection (ICRP) Human Respiratory Tract Model (ICRP, 1994), the NCRP model (NCRP, 1997) and Multiple Path Particle

68 Dosimetry (MPPD) model (Anjilvel and Asgharian, 1995). Different conceptual particle deposition models vary primarily

69 with respect to lung morphometry and mathematical modelling techniques, rather than by using different deposition equations.

70 The three whole lung deposition models define regions of the human lungs (head airway, tracheobronchial and alveolar) for

71 any combination of particle size and breathing pattern (Hofmann, 2009). Among all models, single-path models, such as ICRP

72 model, are often used over multiple-path models due to their simplicity and their applicability to an average path without

73 requiring detailed knowledge of the branching structure of lungs. Owing to a higher potential health risk, LDSA in alveolar

74 region is often of greatest concern and it can be calculated by summing up the products of the surface concentration across

75 particle size spectrum and their corresponding deposition efficiency based on the selected deposition model.

76

77 Apart from numerical computation method, LDSA could also be measured by accredited instruments. Diffusion charging

78 based technique is a common approach where particles are charged with a unipolar corona charger (Fissan et al., 2006). This

79 method enables measurement of ultrafine particles and, more specifically, the LDSA concentration with good accuracy (Todea

80 et al., 2015) and stable performance in long term measurements (Rostedt et al., 2014). Nanoparticle Surface Area Monitor

81 (NSAM) has been used for decades (e.g. Asbach et al., 2009; Hama et al., 2017; Kiriya et al., 2017; Hennig et al., 2018), and

82 several other instruments and sensors, including DiSCmini, Testo Inc. (e.g. Eeftens et al., 2016; Habre et al., 2018) and

83 Partector, Naneos Ltd. (e.g. Cheristanidis et al., 2020), and Pegasor AQ Urban, Pegasor Ltd. (e.g. Kuuluvainen et al., 2018;

84 Kuula et al., 2020), using similar measuring techniques, are developed later on. Using these instruments in campaigns and

85 continuous measurements, LDSA concentrations in alveolar region and size distribution measurements in various

86 environments have been reported across the globe in the past decade (Table 1). When comparing LDSA concentrations

87 measured by different instruments, the instruments' limitations should be considered in experimental LDSA studies, which

88 will be further discussion in Sect. 2.2.

89

90 Although each of these methods is capable of measuring aerosol surface area concentrations, the corresponding uncertainties

91 and cost hinder the widespread use in monitoring networks (Asbach et al., 2017). Even though the instruments are available,

92 missing data often takes place due to instruments maintenance and data corruption. Kuula et al. (2020) demonstrated high

93 correlations of measured LDSA concentrations with black carbon (BC) and nitrogen oxide (NO_x) in traffic environments.

94 Traffic activities have been observed to be significant source contribution to the LDSA concentrations (Järvinen et al., 2015).

95 A clear correlation was also found between the emission factors of exhaust plume BC and LDSA in on-road studies for city

96 buses (e.g. Järvinen et al., 2019). These highly correlating relationships provide good grounds for estimating LDSA

97 concentrations and short-term trends by the other pollutants measured at the same site with the use of data mining-based

98 approach as statistical models. These statistical models can eventually turn into virtual sensors of LDSA after being validated

99 even under the circumstances of no actual instrumental LDSA measurements. Due to the health effects LDSA has

100 demonstrated, it is of great importance to researchers that continuous measurements of LDSA are available with the help of

101 these virtual sensors via statistical models. Similar approach for sensor virtualisation of BC measurement has been studied in

102 Fung et al. (2020).

103

104 Data mining-based approach exploits statistical or machine learning techniques to detect patterns between predictors and

105 dependent variables in the time series data. They do not demand in-depth understanding of air pollutant dynamics, but

106 evaluation by experts is still required to determine whether the models work properly. Simple yet apprehensible models, such

107 as multiple linear regression (MLR, e.g. Fernández-Guisuraga et al., 2016) and generalized additive models (GAM, e.g. Chen

108 et al., 2019), are commonly utilised as white-box models in air pollutant proxy studies. Furthermore, more sophisticated

109 machine learning black-box models, such as artificial neural network (ANN, e.g. Cabaneros et al., 2019; Zaidan et al., 2019;

110 Fung et al., 2021a), nonlinear autoregressive network with exogenous inputs (NARX, e.g. Zaidan et al., 2020) and support

111 vector regression (SVR, e.g. Fung et al., 2021b), have been intensively investigated in recent years. They work better in terms

112 of accuracy; however, they provide limited transparency and accountability regarding the outcomes (Rudin, 2019; Fung et al.,

113 2021b).

114

115 Apart from model structures, the criteria of selecting variables in multipollutant datasets for model development have received

116 considerable attention over the years, and a large number of methods have been proposed (Miller, 2002). Traditional methods,

117 like stepwise procedures, which is a combination of forward selection and backward elimination (e.g. Liu et al., 2018b; Chen

118 et al., 2019), can be unstable because it uses restricted search through the space of potential models, which eventually causes

119 inherent problem of multiple hypothesis testing (Breiman, 1996; Faraway, 2014). Another approach named regularization has

120 emerged as a successful method to reduce the data dimension in an automated way, yet deal poorly with multi-collinear

121 variables, for example Least Absolute Shrinkage and Selection Operator (LASSO, e.g. Fung et al., 2021b; Šimić et al., 2020),

122 ridge regression (e.g. Chen et al., 2019) and ELASTINET (e.g. Chen et al., 2019). Criterion-based procedures, which choose

123 the best predictor variables according to some criteria (e.g. coefficient of determination, residual, etc), are sensitive to outliers

124 and influential points, but involve a wider search and compare models in a preferable manner. Examples are best subset

125 regression (e.g. Chen et al., 2019), input adaptive proxy (IAP, e.g. Fung et al., 2020; Fung et al., 2021b), etc. Hastie et al.

126 (2020) compared some of the models using the three approaches and concluded that no single feature selection method

127 uniformly outweighs the others. Despite the extensive research of feature selection methods, the inclusion of random effects

128 together with the fixed effects as linear mixed-effects (LME) model has received relatively little attention (e.g. Mikkonen et

129 al., 2020; Tong et al., 2020) in air pollution research, let alone LDSA study in particular. This inclusion of random effects

130 could acknowledge a possible effect coming from a factor where specific and fixed values are not of interest.

131

132 In this study, we combine the use of criterion-based feature selection method and the inclusion of random effects, and develop

133 a novel input-adaptive mixed effects (IAME) model to estimate alveolar LDSA concentrations, which is the first study of this

134 context to our best knowledge. The description of LDSA measurements and the techniques of IAME model are outlined in

135 Sect. 2 and 3, respectively. Section 4 presents the characteristics of alveolar LDSA, including its seasonal variability, weekend

136 effect and diurnal pattern, in four types of environments. We also aim to investigate the correlation with other air pollutants.

137 In Sect. 5, we evaluate the performance of the IAME proxy ($LDSA_{IAME}$) with the measured alveolar LDSA by Pegasor AQ

138 Urban ($LDSA_{Pegasor}$), ICRP lung deposition model derived LDSA ($LDSA_{ICRP}$) and another modelled alveolar LDSA by IAP

139 ($LDSA_{IAP}$) as well as the benefits and implication of this alveolar LDSA model as virtual sensors. It should be noted that this

140 study discusses LDSA in alveolar region, unless stated otherwise.

141 **2 Measurement description**

142 **2.1 Measurement sites**

143 We retrieved aerosol, gaseous and meteorological data from two types of measurement sites, i.e., street canyon (SC, 2017–

144 2018) and urban background (UB, 2017–May 2018), in Helsinki Metropolitan Area (HMA) described in more details below.

145 Data from detached housing (DH, 2017) and regional background (RB, 2017) sites were also included in the study to provide

146 comparison and data from the background concentrations. Situated on a relatively flat land at the coast of Gulf of Finland,

147 HMA has land area of 715 km^2 and population of about 1.13 million inhabitants. Helsinki can be classified as continental or

148 marine climate depending on the air flows and the pressure system. Figure S1 and Table S1 show the detailed site description.

149 **Street canyon site (SC)**: Mäkelänkatu urban supersite is operated by the Helsinki Region Environmental Services Authority

150 (HSY, Kuuluvainen et al., 2018). The station is located at 3 km from the city centre in a street canyon in the immediate vicinity

151 to one of the main roads leading to downtown Helsinki. The street, with speed limit of 50 km h^{-1}, consists of six lanes and two

152 tramlines. The annual mean traffic volume in 2018 per workday was 28 100 vehicles, 11% of which were recorded as the

153 heavy duty vehicles. The traffic loads are especially high during rush hours at 8 a.m. and 5 p.m. (Figure S2). The street canyon

154 of width of 42 m is surrounded by rows of buildings of 17 m high, which weaken the dispersion process of the direct vehicular

155 emissions. All the inlets for the measuring devices are positioned approximately at a height of 4 m from the ground level.

156 **Urban background site (UB)**: The Station for Measuring Ecosystem-Atmosphere Relations III (SMEAR III, Järvi et al.,

157 2009) in Kumpula, situated on a rocky hill at 26 m above sea level, is about 4 km northeast from the Helsinki centre. The

158 surroundings of this urban background station are heterogeneous, constituting of residential buildings, small roads, parking

159 lots, patchy forest and low vegetation from different direction. One main road (45 000 vehicles per workday) is located at the

160 distance of 150 m east from the site. Trace gases and meteorological conditions are measured at a height of 4 m and 32 m,

161 respectively, at a triangular lattice tower while aerosol measurements are conducted inside a container approximately 4 m

162 above the ground. The site is co-operated by Finnish Meteorological Institute (FMI) and the University of Helsinki (UHEL).

163 **Detached housing site (DH)**: Three measurement stations, Rekola (DH1), Itä-Hakkila (DH2) and Hiekkaharju (DH3), were

164 chosen since they represent a sub-urban residential area surrounded by detached houses. These sites are mainly affected by the

165 wood combustion emissions from residential activities, especially in cold weather conditions. Emissions from traffic source

166 also account for a small portion of the whole pollution. It is estimated that 90 % of the households burn wood to warm up

167 houses and saunas, less than 2 % of which use wood burning as the main heating source in detached houses in HMA (Hellén

168 et al., 2017).

169 **Regional background site (RB):** The RB site is located about 23 km away from the Helsinki city centre at Luukki, surrounded

170 by a wooded outdoor recreational area right at the edge of the Greater Helsinki golf course. The measuring station is in an

171 open place away from busy traffic routes and large point sources. As a result, this site can represent background concentration

172 levels outside the urban area without any main local sources.

173 **2.2 Instruments**

174 **LDSA measurements:** The sensor unit and the core of the Pegasor AQ Urban is practically another instrument called a Pegasor

175 PPS-M sensor (Pegasor Ltd., Finland) originally designed for automotive exhaust emission measurements (e.g. Maricq, 2013;

176 Amanatidis et al., 2017). The operation of the sensor is based on diffusion charging of particles and the measurement of electric

177 current without the collection of particles. The diffusion charging of particles is carried out by a corona-ionized flow that is

178 mixed with the ambient sample air in an ejector diluter inside the sensor. The sampling lines and the sensor unit are heated to

179 40°C above the ambient temperature (1) to dry the aerosol sample, (2) to prevent interference from humidity, and (3) to prevent

180 any water condensation inside the sensor. The performance of the Pegasor PPS-M sensors for long-term ambient measurements

181 has been improved after they were tested in Helsinki (Järvinen et al., 2015) and Beijing (Dal Maso et al., 2016). The suggestions

182 have been considered for the design of the current form of the Pegasor AQ Urban in this study.

183 The Pegasor AQ Urban (dimension: 320 mm×250 mm×1000 mm), which consists of a weatherproof cover, clean air supply,

184 and the abovementioned Pegasor PPS-M sensor, has been designed such that its response to LDSA is not to be subjected to

185 meteorological fluctuation for outdoor operation. Kuuluvainen et al. (2016) used two Pegasor AQ Urban devices during a 2

186 week period at an urban street canyon and an urban background measurement station in Helsinki, Finland whereas Kuula et

187 al. (2019) later used the instruments in a 3 month long campaign at the same urban street canyon station. These studies

188 demonstrated that the output signal of the Pegasor AQ Urban correlated well with other devices measuring LDSA

189 concentrations such as the Partector and DiSCmini. Kuula et al. (2020) further validated the accuracy and stability of Pegasor

190 AQ Urban at the street canyon station by comparing the measured values of one full year with DMPS reference instruments

191 ($R^2 = 0.90$, $RMSE = 4.1$ μm^2 cm^{-3}). The internal precision of Pegasor AQ Urban is $\pm$ 3%, but this was not tested prior the

192 campaign. The instrument is optimized to measure the alveolar LDSA concentrations of particles in ~10–400 nm size range.

193 Pegasor AQ Urban tends to underestimate LDSA of particle larger than about 400 nm. In typical urban environments, most of

194 the particles from local combustion sources are in the size below the threshold (Asbach et al., 2009; Kuuluvainen et al., 2016;

195 Pirjola et al., 2017), generated vastly by anthropogenic sources such as vehicular exhaust emissions (Karjalainen et al., 2016)

196 and residential wood combustion (Tissari, 2008) which typically produce large amount of small particles. However, the impact

197 of larger particles (>400 nm) to alveolar LDSA might be significant, for example in HMA during $PM_{2.5}$ long-range transport

198 episodes or when there are many particles from very low-quality residential burning in detached housing areas (Pirjola et al.,

199 2017). The regional background source in very polluted regions (e.g. Delhi, Salo et al., 2021a; mining environments, Salo et

200 al., 2021b) could be another reason for the significant impact of larger particles. This limitation of Pegasor AQ Urban should

201 be considered when it comes to data analysis in Sect. 4 and 5.

202 **Aerosol measurements:** Differential mobility particle sizer (DMPS) in combination of a differential mobility analyser (DMA)

203 and a condensation particle counter (CPC) measures aerosol size distribution (Kulkarni et al., 2011). Vienna DMA and

204 Airmodus A20 CPC (measurements of particle size range 6–800 nm) were used at the SC site while a twin DMPS (Hauke-

205 type DMA and TSI Model 3025 CPC + Hauke-type DMA and TSI Model 3010 CPC, merged particle size range 3–1000 nm)

206 were used at the UB site. Both instruments make use of the bipolar charging of aerosol particles, followed by classification of

207 particles into size classes according to their electrical equivalent mobility. In addition to particle size distribution, total particle

208 number concentration (PNC, in cm^{-3}) was calculated by summation. Particle mass concentration of diameter less than 2.5 μm

209 ($PM_{2.5}$, in μg m^{-3}) and less than 10 μm (PM_{10}, in μg m^{-3}) were measured continuously with ambient particulate monitor TEOM

210 1405 at the SC site and TEOM 1405-D at the UB site. Black carbon (BC, in μg m^{-3}) mass concentration was measured by a

211 multi-angle absorption photometer (MAAP) Thermo Scientific 5012 with a PM$_1$ inlet. The measured absorbance was converted

212 to BC mass concentration by using a fixed 6.6 m^2 g^{-1} mass absorption coefficient at wavelength of 637 nm. PM$_{2.5}$, PM$_{10}$ and

213 BC were recorded in µg m^{-3}.

214 **Ancillary measurements:** Trace gas concentrations (in ppb), including nitric oxide (NO), nitrogen dioxide (NO$_2$), their sum

215 nitrogen oxide (NO$_x$), ozone (O$_3$) and carbon monoxide (CO) were determined with a suite of gas analysers. In addition,

216 supporting meteorological variables, including air temperature (Temp), relative humidity (RH), air pressure (P), wind speed

217 (WS), wind direction (WD) and photosynthetically active radiation (PAR), were measured at SC and UB. Figure S3 show the

218 meteorological conditions during the measurement period. A list of collected variables is shown in Table S2.

3. Method

3.1 Data pre-processing

221 The collected data was quality checked by the corresponding operating organisation, HSY, FMI and UHEL. No additional

222 pre-processing was done for general analysis. For proxy development, outliers due to potential measurement errors were

223 detected (SC: 0.73%; UB: 0.99% overall) by using the interquartile range (IQR) rule, which is applicable for non-Gaussian

224 distribution sample. We calculated the cut-off for outliers as 2 times the IQR, subtracted this cut-off from the 25th percentile

225 and added it to the 75th percentile to give the actual limits on the data. We applied a natural logarithm transformation to all the

226 skewed-distributed aerosol and trace gases measurements in order to keep the distribution of each parameter following a normal

227 distribution. Since wind direction is a circular variable, it is resolved into North-South (WD–N) and East-West (WD–E) vector

228 components by trigonometric functions.

3.2 Size-fractionated lung deposited surface area (LDSA$_{ICRP}$)

230 Alveolar deposition fraction (DF_{AL}) as a function of particle size with the unit density is determined with the ICRP Human

231 Respiratory Tract Model by the following equation (ICRP, 1994):

$$DF_{AL} = \left(\frac{0.0155}{d_p}\right)\left(\exp\left(-0.416\left(\ln d_p + 2.84\right)^2\right) + 19.11 \exp\left(-0.482\left(\ln d_p - 1.362\right)^2\right)\right) \tag{1,}$$

232 where d_p is the aerodynamic diameter (µm) of spherical particles with the unit density (1 g cm^{-3}). The equation is determined

233 in two parts with respect to the two different peaks in the deposition curve in Figure 1. The peak near the size of 20 nm can be

234 approximated to represent the Brownian deposition, whereas the peak between 1 µm and 2 µm represents the inertial

235 deposition. From the particle number size distribution, we calculated the particle surface area distribution assuming each

236 particle is monodisperse sphere of standard density at standard conditions. By Eq. (1), a deposition factor for each particle size

237 bin (26 size bins at SC and 49 at UB) were calculated. Size-fractionated LDSA was then computed by multiplying the surface

238 area concentration with DF_{AL} in the corresponding size class. Total LDSA calculated by the ICRP lung model (LDSA$_{ICRP}$) can

239 be obtained by summing up the all the size-fractionated LDSA values (Hinds, 1999). In this study, the alveolar LDSA$_{ICRP}$ was

240 calculated based on DMPS measurements in SC and UB. Thus, while the alveolar LDSA measured by Pegasor (LDSA$_{Pegasor}$)

241 represent the ~10–400 nm size range, the alveolar LDSA$_{ICRP}$ represent 6–800 nm and 3–1000 nm size range in SC and UB,

242 respectively.

3.3 Novel Input-adaptive mixed-effects (IAME) model

244 Input-adaptive mixed-effects (IAME) model is a combination of input-adaptive proxy (IAP) and linear mixed-effects (LME)

245 model. IAP was first introduced by Fung et al. (2020) and has been demonstrated reliable and flexible to fill up missing values

246 by taking input variables adaptively with robust ordinary least square regression models. IAP has been able to estimate BC

247 concentration by other air quality indicators with a satisfactory performance in two different categorised urban environments,

248   street canyon (adjusted $R^2 = 0.86$–0.94) and urban background (adjusted $R^2 = 0.74$–0.91). Some models outperformed IAP in

249   accuracy performance, but its transparent model structure and ability to impute missing values still make it a preferred option

250   as a virtual sensor (Fung et al., 2021b).

251

252   In this study, we primarily stuck to the strength to select input variables adaptively with the introduction of mixed effects. The

253   mixed effect approach is a generalization of the linear model that can incorporate both fixed (i.e. causing a main

254   effect/interaction) and random effects (i.e. causing variance/variability in responses), allowing the account of several sources

255   of variations (Chudnovsky et al., 2012). As seen in Figure 2, we picked the direct air pollutant measurement from the station

256   (variables of high correlation: $PM_{2.5}$, BC and NO_2 and other supporting variables: PM_{10}, O_3, NO_x, NO, CO and PNC) and

257   meteorological data of higher correlation (Temp, RH, P, PAR, WS, WD–N, WD–E) as the fixed variables because the air

258   pollutants can indicate the sources of LDSA which largely come from combustion and meteorological data could influence the

259   dispersion and dilution of LDSA. They are the most direct factors to the fluctuation of LDSA concentrations. Due to the strong

260   seasonal variation, weekend effects and diurnal pattern in urban air pollutant concentrations (Fung et al., 2020), the variance

261   in responses might depend on the time indicators that are not the primary cause of the concentration variability, but they

262   indirectly alter human-induced activities, such as traffic amounts. To take them into account, we created three time hierarchical

263   sub-groups (12 months of year, 7 days of week and 24 hours of day) as the inputs of random effect variables.

264

265   The regression equation of IAME is similar to the equation of IAP, except that IAME includes additional intercepts term for

266   random effects as below:

$$y_i = \beta_0 + \sum_{k=1}^{p} \beta_{ik} x_{ik} + \sum_{j=1}^{q} b_{ij} + e_i$$

(2),

267   where y_i is the ith estimated LDSA concentration. The first term on the right β_0 indicates the fixed intercept of the equation.

268   The second term represents the total contribution by the direct measurement of variable x as fixed effects with a slope β at

269   each data point i. A maximum of three inputs from the total 16 fixed variables are selected to from 696 sub-models (Figure 2).

270   The inputs for random effects are indicated by b as intercepts of the corresponding three hierarchical sub-groups. A Gaussian

271   error term is indicated by e. The explanation of Eq. (2), is visualised in Figure 2.

272

273   One of the assumptions of LME models is that the random effects, together with the error term, have the following prior

274   distribution:

$$b \sim N\big(0, \sigma^2 D(\theta)\big)$$

(3),

275   where D is a q-by-q symmetric and positive semidefinite matrix, parameterized by a variance component vector θ, q is the

276   number of variables in the random-effects term, and σ^2 is the observation error variance. We use an optimiser, restricted

277   maximum likelihood, commonly known as ReML, with the value 1×10^{-6} as the relative tolerance on gradient of objective

278   function and 1×10^{-12} as absolute tolerance on step size. The use of ReML over the conventional ML could produce unbiased

279   estimates of variance and covariance parameters (Lindstrom and Bates, 1988).

280

281   After the sub-model formation, the dataset was randomly divided into five portions. 80% of the data were allocated for 4-fold

282   cross validation to remove variance of accuracy. The results of all the folds were averaged and the sub-models were ranked by

283   several evaluation metrics, which were further demonstrated in Figure 2 and described in Sect. 3.4. Some of the sub-models

284   were subject to rejection under two conditions: (1) strong multi-collinearity among the fixed parameters (variance inflation

285   factor (VIF) > 5) and (2) violation of the normality assumption of residuals also known as heteroscedasticity (fail in

286   Kolmogorov-Smirnov (K-S) test, $p < 0.05$). Based on the situation of missing data, the automatised IAME model would search

287 for the best sub-model option from the ranking chart. Hence, each data point might be estimated differently depending on the

288 available data. The number of data points being estimated by each sub-model was reported to show their frequency of usage.

3.4 Evaluation metrics

290 In order to evaluate the model performance quantitatively, we used the following metrics:

$$R^2 = 1 - \frac{\sum_{i=1}^{N}(y_i - \widehat{y_i})^2}{\sum_{i=1}^{N}(y_i - \bar{y})^2} \tag{4},$$

$$MAE = \frac{1}{N}\sum_{i=1}^{N}|y_i - \widehat{y_i}| \tag{5},$$

$$cRMSD = \sqrt{\frac{1}{N}\sum_{i=1}^{N}((y_i - \bar{y}) - (\widehat{y_i} - \tilde{y}))^2} \tag{6},$$

$$r = \frac{\sum_{i=1}^{N}(y_i - \bar{y})(\widehat{y_i} - \tilde{y})}{\sqrt{\sum_{i=1}^{N}(y_i - \bar{y})^2}\sqrt{\sum_{i=1}^{N}(\widehat{y_i} - \tilde{y})^2}} \tag{7},$$

$$NSD = \frac{SD_{predicted}}{SD_{reference}} = \frac{\sqrt{\frac{1}{N-1}\sum_{i=1}^{N}(\widehat{y_i} - \tilde{y})^2}}{\sqrt{\frac{1}{N-1}\sum_{i=1}^{N}(y_i - \bar{y})^2}} = \sqrt{\frac{\sum_{i=1}^{N}(\widehat{y_i} - \tilde{y})^2}{\sum_{i=1}^{N}(y_i - \bar{y})^2}} \tag{8},$$

291 where $\widehat{y_i}$ and $\widehat{y_i}$ are i^{th} measured data point and estimated variable by the model, respectively. $\bar{y}$ and $\tilde{y}$ are the expected value

292 of the measured and modelled dataset, respectively. N is the number of complete data input to the model. Coefficient of

293 determination (R^2) is a measure of how close the data lie to the fitted regression line. It, however, does not consider the biases

294 in the estimation. Therefore, we further validated the models with mean absolute error (MAE) and centred root-mean-square

295 differences ($cRMSD$), where MAE measures the arithmetic mean of the absolute differences between the members of each

296 pair, whilst $cRMSD$ calculates the square root of the average squared difference between the forecast and the observation pairs.

297 $cRMSD$ is more sensitive to larger errors than MAE. Furthermore, together with $cRMSD$, Pearson correlation coefficient (r)

298 and normalised standard deviation (NSD) of the modelled data set are also studied. r describes the correlation between the

299 measured and modelled data whereas NSD measures the relative spread of the data. Due to their unique mathematical

300 relationship, the three metrics can be portrayed on Taylor's diagram, which has been used for sub-model selection purpose.

301 We ranked our sub-models first by R^2, followed by MAE and $cRMSD$. r and NSD serve as additional evidence when we

302 explain the model performance.

3.5 Two-sample t-tests

304 We assessed the temporal and spatial impact on the IAME model by comparing the means of absolute differences between the

305 hourly measured and modelled LDSA in different time windows at both stations. Two-sample t-tests were performed on the

306 two populations of absolute differences abovementioned to determine whether the difference between these was statistically

307 significant. A significance level α of 5% was chosen as the probability of rejecting the null hypothesis when it is true, denoted

308 as p.

4 LDSA measurement characterization

4.1 General characteristics of LDSA_Pegasor in Helsinki metropolitan area

311 The annual mean alveolar LDSA concentrations at four station types SC (2017–2018), UB (2017–May 2018), DH (2018) and

312 RB (2018) were 19.7±11.3 µm² cm⁻³, 11.2±7.1 µm² cm⁻³, 11.7±8.6 µm² cm⁻³ and 7.6±5.4 µm² cm⁻³, respectively (Table 2).

313 The DH and RB site were included to give more substantial interpretation of data because the LDSA concentrations at RB can

be viewed as background measurements and the local LDSA increments in HMA can be represented by the LDSA at the hotspot measurement site subtracted by the LDSA at the RB site. The timeseries of LDSA concentrations at the SC and the UB site were presented in Figure 3 and Fig. S4, where the missing data of LDSA for the whole measurement period was 3% and 30%, respectively. When comparing with the same site type in other cities around the globe, LDSA concentrations detected in HMA were the lowest among the European cities with reported values. While some literatures also reported LDSA at tracheobronchial region, most just considered LDSA at alveolar, which is considered to bring most harm to human's lungs, as shown in Table 1.

The diurnal pattern of LDSA at RB was not observable on workdays or over weekends (Figure 4, upper panel). The relatively low variability can be explained by the scarcity of human activities. We can then regard the LDSA at RB as the background concentrations mainly influenced by the regionally and long-range transported aerosol and meteorological variation (see Luoma et al., 2021; Jafar and Harrison, 2021). As the concentrations at RB was stable throughout the different hours of day; therefore, the diurnal pattern of LDSA concentration was apparently indistinguishable between the measured concentration and the local increments. At the UB and DH site, the magnitudes and the patterns of the average hourly LDSA concentrations at workdays were comparable, and both showed bimodal curves, one peak at 6−9 a.m., the other at 9−11 p.m.. The former had a larger peak during the morning peak hour because of the vehicular emissions (Timonen et al., 2013; Teinilä et al., 2019) while the latter had a larger peak in the evening attributed mainly by the residential burning (Hellén et al., 2017; Helin et al., 2018; Luoma et al., 2021). Over weekends, the peaks in the morning were not identifiable and the evening peaks were amplified due to enhanced human activities. Similar diurnal variation at residential area was observed for BC emitted by residential combustion by Helin et al. (2018). At the SC site, the morning peak on weekends was not obvious because of the lack of work-related traffic. It appears that a similar bimodal curve can be seen during workdays, but the evening peak was seen during the evening traffic rush hour around 4−6 p.m.. The reason was that the main contributor of LDSA at the SC site was traffic and combustion processes and the diurnal variability mainly depended on the citizen's movement by vehicles in the city. Over weekends, the average hourly LDSA concentrations were the minimum at 5 a.m. and they increased and remained at a high level at 2 p.m. until the late night. The level of LDSA concentrations at DH was comparable with that at UB site. However, the amplitude of the evening peak was higher than that of the morning peak both on workdays and weekends due to elevated residential combustion.

However, the monthly variability of background measurements at the RB site was stronger compared to the diurnal pattern and the calculation of local increment was necessary (e.g. Jafar and Harrison, 2021). With no intense point sources, the variations at RB were probably due to horizontal dispersion and advection of aerosol particles and vertical dilution controlled by the boundary layer dynamics. Based on the monthly frequencies of backward trajectory by NOAA HYSPLIT Trajectory Model (Rolph et al., 2017, Fig. S5), pollutants could be originated 600 km away from Helsinki within 24 hours in the winter. In the summer, when solar radiation was persistently stronger, the boundary layer became elevated due to surface heating and associated thermal turbulence. This turbulence would dilute the concentration of pollutants at the surface. Another plausible reason could be the higher regional and long-range transported LDSA in the summer, as demonstrated by Kuula et al. (2020) and Barreira et al. (2021). The lower panel in Figure 4 shows the LDSA local increments after subtraction of the LDSA concentrations at the RB site. For instance, the local LDSA increments at DH are the highest in the winter probably due to local small-scale wood combustion (and traffic). However, without subtracting the background concentrations, the LDSA concentrations at DH were higher in the summer than in the winter (due to high regional background concentrations in summer), as was observed also by Kuula et al. (2020). This piece of evidence can help in the source apportionment. The variation of diurnal and seasonal LDSA for all sites are visualised in Fig. S6.

4.2 The connection between LDSA and other parameters

Alveolar LDSA concentration, as a single number, comprises particles across the whole particle size spectrum measured (e.g. Pegasor AQ Urban ~10–400 nm). In HMA, the two local main sources of particles contributing to LDSA are vehicular combustion and residential wood combustion emissions. Upon the two combustion processes, particles of different sizes and different gaseous pollutants are emitted. A study by Lamberg et al. (2011) has shown that the geometric mean diameter of residential wood combustion is typically 70–150 nm whereas Barreira et al. (2021) presented that the typical particle size for vehicular combustion can be smaller than 50 nm. By calculating the proportion of LDSA with respect to different pollutant parameters BC, NO_x, PNC (dominated by UFP), and $PM_{2.5}$, we could identify the contribution of LDSA across the hour of day (Fig. S7 for workdays and Fig. S8 for weekends). Since the vehicular combustion emits smaller particles which elevate the LDSA concentration but meanwhile do not substantially influence the value of $PM_{2.5}$ (e.g. Salo et al., 2021a); therefore, $LDSA/PM_{2.5}$ had a diurnal pattern similar to the LDSA concentrations which peaked in the morning rush hour during workdays. Conversely, LDSA/BC, LDSA/PNC and $LDSA/NO_x$ had a higher value before the morning rush hour and they plunged in the morning rush hour. This can be explained by the fact that vehicular combustion caused high concentration of BC, PNC and NO_x (Reche et al., 2015) compared to its contribution to LDSA concentration. In other words, the role of regional background was higher for LDSA compared to those of NO_x, BC and PNC. At the UB site, the average LDSA/BC at all hours remained at a constant level in the winter while the variability of the ratio was much higher in the summer. The general LDSA/PNC ratio at UB was steadily 2−3 times higher than that at all hours in all seasons because the proportion of larger particles at UB was usually higher than SC. This large variability again validated the heterogeneity of source of LDSA at UB.

The integrated alveolar LDSA with a various size ranges was calculated to explore the correlation of size-fractionated LDSA and other parameters in our multipollutant dataset. No single fractionated LDSA correlated well with meteorological parameters at both sites (Figure 5). Out of all fractions, alveolar LDSA of the whole spectrum ($LDSA_{6–800}$) and $LDSA_{250–400}$, which explained majority of LDSA, correlated best with other air pollutants. In general, alveolar LDSA had a high correlation with BC. BC correlated the best with $LDSA_{100–250}$ ($r = 0.84$), which was in alignment with the reported values from previous literatures (Gramsch et al., 2014; Ding et al., 2016). As expected, $PM_{2.5}$ showed better correlation with the LDSA of larger particles ($r = 0.68−0.76$) because larger particles contributes more to $PM_{2.5}$ mass concentration values. In the meanwhile, PM_{10} had fair correlation with all selected size bins. NO_2 correlated highly with LDSA of smaller particles ($r = 0.69−0.77$), indicating the dominant role of local traffic exhausts. CO had a higher correlation with LDSA of $400−800$ nm ($r = 0.64$) since CO concentrations were more affected by regionally transported pollutants. O_3 had a fair correlation with LDSA of all sections ($r = 0.30−0.43$) because the formation of O_3 is mostly secondary and the chemical interactions with pollutants are more complicated than the other compounds. In general, the correlations of LDSA with other air pollutant parameters were higher at the SC site than that at the UB site (Fig. S9). The high correlations of LDSA with BC, $PM_{2.5}$ and NO_2, which agreed with the results by Kuula et al. (2020), proved the possibility of developing a model to estimate LDSA concentrations.

5 Model evaluation

5.1 Sub-model diagnostics

Following the evaluation attributes described in Sect. 3.4,

Table 3 depicts the descriptive statistics of the overall model evaluation on its testing set. The overall model at the SC site was able to explain 80% of the variability of the testing set of the measured data. The R^2 in the winter was 0.86 being the highest while the worst R^2 was shown in the summer, i.e., 0.70. The MAE and $cRMSD$ were the smallest during weekends with R^2 not particularly high ($R^2 = 0.72$) probably because the LDSA concentration itself was relatively low in that period. The overall performance was generally worse in UB in terms of R^2, except during weekends that R^2 is 10% higher.

For individual sub-models, their performance could be seen on the Taylor's diagram in Figure 6 (Taylor, 2001). Each marker represents one sub-model, the contribution of which to the outcome of the final model is displayed in various colours. The sub-model performance can be evaluated by the distance of the sub-model marker and the red point, which represents the reference station, i.e., the perfect model. The location of each marker indicates its individual performance in terms of r (blue contours), $cRMSD$ (green contour) and NSD (black axis). At the SC site, the narrow distribution of the sub-models on the Taylor's diagram gives a clue that they were very similar in terms of model performance of LDSA estimation. The five mostly used sub-models were concentrated within the region where r was 0.85–0.87, $cRMSD$ was 5.67−5.77 µm^2 cm^{-3} and NSD was 0.75−0.79 (Table 4). The values of their evaluation metrics were close to each other where R^2 and MAE differed in the narrow range of 10% ($R^2 = 0.72$–0.74, $MAE = 3.8$ µm^2 cm^{-3}). It infers that if one metric was prioritised over another, the rank of the sub-models can be greatly different. Although no individual sub-models showed r greater than 0.9, the overall model comprising the outcomes by all the sub-models remained high ($R^2 = 0.80$, $MAE = 3.8$ µm^2 cm^{-3}). The best sub-model was also the most used one, which accounted for 81% of the total data points while the two succeeding sub-models constituted another 16%. This also indicates that the input adaptivity function of the suggested method supplemented 19% of the estimates, which would be a missing estimate if a single model with fixed predictor variables was used. Four out of the five most used sub-models contain BC as an input predictor with the combination of other two air pollutants or meteorological parameters. This was in line with the high correlation of LDSA with BC ($r = 0.84$, Fig. S9) In case BC is missing at a certain time stamp, the sub-model without BC as an input could be used. It further supports the input adaptive function.

At the UB site, the sub-model performance was more scattered on the Taylor's diagram (Figure 6). The five most used sub-models had varying metrics ($r = 0.77−0.92$, $cRMSD = 2.5−3.9$ µm^2 cm^{-3} and $NSD = 0.63−0.89$, see Table 5). Although some showed exceptionally good performance, the overall model had a slightly worse performance than that in street canyon. The best sub-model estimated 49% of the total measurement, followed by 17%. The third and fourth most used sub-models, which formed up to 30% of the estimates, had rather moderate performance ($R^2 = 0.58$ and 0.69). Considering all possible outcomes, the overall model was still able to explain 77% of the total variance. Despite the fair linear correlation with LDSA, CO ($r = 0.26$) and PNC ($r = 0.71$) dominated in the top five used sub-models. This could be explained by the fact that the source of CO can well cover the missing piece that PNC was unable to account for LDSA. BC, NO$_x$ and meteorological parameters, like RH and WD-N were also involved in the final LDSA estimation.

By checking the variance inflation factor (VIF) of all 696 sub-models, 4.6% and 2.2% were rejected respectively. The higher rejection rate at SC can be explained by the fact that some of the predictor variables were highly correlating to each other and the inclusion of them would result in an inflation of multi-collinearity of the sub-model, from which biases arose. At UB, since the source of LDSA was more varied and the correlation of LDSA with other pollutants was generally lower, the probability of the VIF of the individual sub-models exceeding the threshold was lower.

5.2 Temporal difference in comparison with other models

Figure 7 presents the comparison of measured LDSA (LDSA$_{Pegasor}$), deposition model derived LDSA (LDSA$_{ICRP}$) and the LDSA modelled by IAP and IAME (LDSA$_{IAP}$ and LDSA$_{IAME}$) as a timeseries plot between 14 and 28 February 2017. This

434 particular time window was selected because it had the least data gaps for all the respective instruments at both sites. This

435 figure during this period can also showcase the difference in magnitudes of the diurnal shape over workdays and weekends

436 (shaded regions in Figure 7). At both sites, both IAP and IAME underestimated the peaks when the change of the measured

437 LDSA concentration was sudden and relatively large. However, this limitation did not diminish much of the usefulness of the

438 models as virtual sensors as the models were still able to generally catch up with the diurnal cycle of the measured data. Despite

439 the small difference observed in the figure, the blue dotted line representing $LDSA_{IAME}$ often stays closer to the measured

440 LDSA concentration (black line). When we smoothed out all the estimates at each hour, the ability for IAME to catch the

441 morning peak on workdays was much better.

442

443 A more generalised diurnal cycle can be found in Figure 8. The error bars of the modelled $LDSA_{IAP}$ and $LDSA_{IAME}$ were

444 consistently smaller than that of $LDSA_{Pegasor}$ and $LDSA_{ICRP}$. It might be due to the reason that the model fails to catch the

445 extreme values although it managed to catch the general diurnal cycle. Since outliers were removed in the pre-processing stage

446 and the model penalised the extreme values, the model tended to give a more centralised estimate. It was a trade-off between

447 the option with better coefficients of determination but stronger extreme errors and that with better estimations at tails but

448 derivation of averaged estimation. This circumstance was more apparent on workdays than weekends. Furthermore, $LDSA_{IAME}$

449 could follow the diurnal cycle of $LDSA_{Pegasor}$ much better than $LDSA_{IAP}$, especially during the start of the peak hours over

450 workdays at the SC site where the LDSA concentrations jumped to a high level. $LDSA_{IAME}$ can explain 80% and 77% of the

451 variability of the reference measurements at SC and UB, respectively (Table 6), and compared to $LDSA_{IAP}$'s 77% and 66%,

452 $LDSA_{IAME}$ performed better in terms of accuracy. In addition, the slightly smaller *MAE* and the closer to 1 *NSD* of the

453 $LDSA_{IAME}$ suggested that the mean absolute error was improved and the spread of the estimation distribution was closer to the

454 reference measurement by taking random effects into account.

455

456 Furthermore, we assessed the temporal and spatial impact on the IAME model by comparing the means of absolute differences

457 between the hourly $LDSA_{Pegasor}$ and $LDSA_{IAME}$ in different time windows at both stations. A descriptive statistic is presented

458 in Table 7. We used two-sample t-tests to assess whether the distribution of absolute differences were statistically significant.

459 At SC, the *p* value of the t-tests at all selected windows were below 0.05, which demonstrated that the performance at different

460 seasons, days of week and hours of day of absolute differences between the measured and modelled LDSA were significantly

461 different at the confidential level of 95%. At the UB site, the difference between the two selected hour periods was not

462 statistically significant. The same applied to the difference between winter and spring. There was no statistically sufficient

463 evidence to validate the difference among the rest of the selected time period. In other words, with the use of random effects

464 of time constraint, the overall models still performed differently at different time windows most of the time. This indicates that

465 IAME still needs improvements on minimising temporal differences.

466 **6 Conclusion**

467 In this study, we developed a novel input-adaptive mixed-effects (IAME) proxy, to estimate alveolar LDSA by other already

468 existing air pollutant variables and meteorological conditions in Helsinki Metropolitan Area. During the measurement period

469 2017–2018, we retrieved LDSA measurements measured by Pegasor AQ Urban (alveolar LDSA in the ~10−400 size range)

470 and other variables in a street canyon (SC, average LDSA = 19.7±11.3 µm^2 cm^{-3}) site and an urban background (UB, average

471 LDSA = 11.2±7.1 µm^2 cm^{-3}) site in Helsinki, Finland. Furthermore, three detached housing sites (DH, average LDSA =

472 11.7±8.6 µm^2 cm^{-3}) and a regional background site (RB, average LDSA = 7.6±5.4 µm^2 cm^{-3}) were also included as reference

473 and background source estimation, respectively. At the SC site, LDSA concentrations were closely correlated with traffic

474 emission. The ratio to black carbon (LDSA/BC), to particle number concentration (LDSA/PNC), and to nitrogen oxide

475 (LDSA/NO$_x$) had a higher value before the morning peak and it reached its minimum during the morning peak since the role

476 of regional background was higher for LDSA compared to those of NO$_x$, BC and PNC. However, the ratio of LDSA to mass

477 concentration of particles of diameter smaller than 2.5 µm (LDSA/PM$_{2.5}$) performed differently since the freshly vehicular

478 emitted particles were smaller than 50 nm, which did not contribute much to PM$_{2.5}$ mass concentration.

479

480 For the continuous estimation of LDSA, IAME was automatised to select the best combination of input variables, including a

481 maximum of three fixed effect variables and three time indictors as random effect variables. Altogether, 696 sub-models were

482 generated and ranked by the coefficient of determination (R^2), mean absolute error (MAE) and centred root-mean-square

483 differences ($cRMSD$) in order. At the SC site, LDSA concentrations can be best estimated by PM$_{2.5}$, PNC and BC, all of which

484 were closely connected with the vehicular emissions, while they were found correlating with PM$_{2.5}$, BC and carbon monoxide

485 (CO) the best at the UB site. At both sites, PM$_{2.5}$ also indicated the regionally and long-range transported pollutants, which

486 was a significant source of LDSA concentrations. The accuracy of the overall model was higher at the SC site (R^2 = 0.80,

487 MAE = 3.7 µm^2 cm^{-3}) than at the UB site (R^2 = 0.77, MAE = 2.3 µm^2 cm^{-3}) plausibly because the LDSA source was more

488 tightly controlled by the close-by vehicular emission source. This model could catch the temporal pattern of LDSA; however,

489 the two-sample t-tests of the residuals at all selected time windows showed that their distributions were different. This indicated

490 that the model still performed differently at different time windows. Despite this, the novel IMAE model worked better in

491 explaining the variability of the measurements than the previously suggested IAP model as indicted by a higher R^2 and

492 lower MAE in both sites. This adjustment by taking random effects into account improved the sensitivity and the accuracy of

493 the fixed effect model IAP.

494

495 The models alone cannot replace the need for reference measurements (Hagler et al., 2018). However, the IAME proxy could

496 serve as virtual sensors to complement the measurements at reference stations in case of missing data. The two measurement

497 sites in this study served as a pilot of the proxy development, and the next step is to extend the work to the existing network

498 of several measurement stations within the Helsinki metropolitan region. With similar configurations, we could fill up the

499 voids with the information from the other stations after conscientious calibration. For example, in this paper, the two

500 measurement sites were characterised as street canyon and urban background. In a different setup, we may assume the

501 similarity of the same type of environment and utilise the measurements as replacement. Furthermore, this continuous LDSA

502 estimation could be useful in updating some of the current air quality application, for instance ENFUSER air quality model

503 which provide accurate spatio-temporal estimation for air pollutants in Helsinki (Johansson et al., 2015).

504 **Data availability**

505 The air quality data and meteorological data are available from HSY website (https://www.hsy.fi/avoindata) and through

506 SmartSMEAR online tool (https://smear.avaa.csc.fi/).

507 **Author contributions**

508 PLF performed formal analysis and writing – original draft of the manuscript. PLF, MAZ, TP and TH conceptualized and

509 designed the methodology of this work. MAZ, ST, MK, TP and TH provided supervision in this research activity. ES (Pegasor

510 Ltd.), JVN and AKo (HSY), and HT, JK and AKa (FMI) provided instruments and data for the campaign. All the co-authors

511 (MAZ, JVN, ES, HT, AKo, JK, TR, Aka, ST, MK, TP and TH) reviewed and commented on the manuscript.

Competing interests

Prof. Markku Kulmala and Prof. Tuukka Petäjä are members of the editorial board of the journal Atmospheric Chemistry and Physics. Dr. Erkka Saukko works in Pegasor Ltd. which is the manufacturer of Pegasor AQ Urban.

Acknowledgements

The authors acknowledge the City of Helsinki for providing traffic count data.

Financial support

This work is supported by the European Regional Development Fund through the Urban Innovative Action (project HOPE; Healthy Outdoor Premises for Everyone, project no. UIA03-240) and Regional Innovations and Experimentations Fund AIKO, governed by the Helsinki Regional Council (project HAQT; Helsinki Air Quality Testbed, project no. AIKO014). Grants are also received from the European Research Council through the European Union's Horizon 2020 Research and Innovation Framework Program (grant agreement no. 742206), and ERA-PLANET (www.era-planet.eu) and its trans-national project SMURBS (www.smurbs.eu) funded under the same program (grant agreement no. 689443). The authors show gratitude to Academy of Finland for the funding via the Academy of Finland Flagship funding (project no. 337549 and 337552) and NanoBioMass (project no. 1307537).

References

Albuquerque, P. C., Gomes, J. F., and Bordado, J. C.: Assessment of exposure to airborne ultrafine particles in the urban environment of Lisbon, Portugal, J. Air Waste Manag. Assoc., 62, 373-380, https://doi.org/10.1080/10962247.2012.658957, 2012.

Amanatidis, S., Maricq, M. M., Ntziachristos, L., and Samaras, Z.: Application of the dual Pegasor Particle Sensor to real-time measurement of motor vehicle exhaust PM, J. Aerosol Sci., 103, 93-104, https://doi.org/10.1016/j.jaerosci.2016.10.005, 2017.

Anjilvel, S., and Asgharian, B.: A multiple-path model of particle deposition in the rat lung, Fund. Appl. Toxicol., 28, 41-50, https://doi.org/10.1006/faat.1995.1144, 1995.

Asbach, C., Fissan, H., Stahlmecke, B., Kuhlbusch, T., and Pui, D.: Conceptual limitations and extensions of lung-deposited Nanoparticle Surface Area Monitor (NSAM), J. Nanopart. Res., 11, 101-109, https://doi.org/10.1007/s11051-008-9479-8, 2009.

Asbach, C., Alexander, C., Clavaguera, S., Dahmann, D., Dozol, H., Faure, B., Fierz, M., Fontana, L., Iavicoli, I., Kaminski, H., MacCalman, L., Meyer-Plath, A., Simonow, B., van Tongeren, M., and Todea, A. M.: Review of measurement techniques and methods for assessing personal exposure to airborne nanomaterials in workplaces, Sci. Total Environ., 603, 793-806, https://doi.org/10.1016/j.scitotenv.2017.03.049, 2017.

Barreira, L. M. F., Helin, A., Aurela, M., Teinilä, K., Friman, M., Kangas, L., Niemi, J. V., Portin, H., Kousa, A., Pirjola, L., Rönkkö, T., Saarikoski, S., and Timonen, H.: In-depth characterization of submicron particulate matter inter-annual variations at a street canyon site in northern Europe, Atmos. Chem. Phys., 21, 6297-6314, https://doi.org/10.5194/acp-21-6297-2021, 2021.

Breiman, L.: Heuristics of instability and stabilization in model selection, Ann. Stat., 24, 2350-2383, https://doi.org/10.1214/aos/1032181158, 1996.

Brown, D. M., Wilson, M. R., MacNee, W., Stone, V., and Donaldson, K.: Size-dependent proinflammatory effects of ultrafine polystyrene particles: a role for surface area and oxidative stress in the enhanced activity of ultrafines, Toxicol. Appl. Pharm., 175, 191-199, https://doi.org/10.1006/taap.2001.9240, 2001.

Buonanno, G., Marini, S., Morawska, L., and Fuoco, F. C.: Individual dose and exposure of Italian children to ultrafine particles, Sci. Total Environ., 438, 271-277, https://doi.org/10.1016/j.scitotenv.2012.08.074, 2012.

Cabaneros, S. M., Calautit, J. K., and Hughes, B. R.: A review of artificial neural network models for ambient air pollution prediction, Environ. Modell. Softw., 119, 285-304, https://doi.org/10.1016/j.envsoft.2019.06.014, 2019.

Chen, J., de Hoogh, K., Gulliver, J., Hoffmann, B., Hertel, O., Ketzel, M., Bauwelinck, M., van Donkelaar, A., Hvidtfeldt, U. A., Katsouyanni, K., Janssen, N. A. H., Martin, R. V., Samoli, E., Schwartz, P. E., Stafoggia, M., Bellander, T., Strak, M., Wolf, K., Vienneau, D., Vermeulen, R., Brunekreef, B., and Hoek, G.: A comparison of linear regression, regularization, and machine learning algorithms to develop Europe-wide spatial models of fine particles and nitrogen dioxide, Environ. Int., 130, 104934, https://doi.org/10.1016/j.envint.2019.104934, 2019.

Cheristanidis, S., Grivas, G., and Chaloulakou, A.: Determination of total and lung-deposited particle surface area concentrations, in central Athens, Greece, Environ. Monit. Assess., 192, 627, https://doi.org/10.1007/s10661-020-08569-8, 2020.

Chudnovsky, A. A., Lee, H. J., Kostinski, A., Kotlov, T., and Koutrakis, P.: Prediction of daily fine particulate matter concentrations using aerosol optical depth retrievals from the Geostationary Operational Environmental Satellite (GOES), J. Air Waste Manag. Assoc., 62, 1022-1031, https://doi.org/10.1080/10962247.2012.695321, 2012.

Dal Maso, M., Gao, J., Järvinen, A., Li, H., Luo, D., Janka, K., and Rönkkö, T.: Improving urban air quality measurements by a diffusion charger based electrical particle sensors-A field study in Beijing, China, Aerosol Air Qual. Res., 16, 3001-3011, https://doi.org/10.4209/aaqr.2015.09.0546, 2016.

Ding, A., Huang, X., Nie, W., Sun, J., Kerminen, V. M., Petäjä, T., Su, H., Cheng, Y., Yang, X. Q., and Wang, M.: Enhanced haze pollution by black carbon in megacities in China, Geophys. Res. Lett., 43, 2873-2879, https://doi.org/10.1002/2016GL067745, 2016.

Dockery, D. W., Pope, C. A., Xu, X., Spengler, J. D., Ware, J. H., Fay, M. E., Ferris Jr, B. G., and Speizer, F. E.: An association between air pollution and mortality in six US cities, New Engl. J. Med., 329, 1753-1759, https://doi.org/10.1056/NEJM199312093292401, 1993.

Duffin, R., Tran, C., Clouter, A., Brown, D., MacNee, W., Stone, V., and Donaldson, K.: The importance of surface area and specific reactivity in the acute pulmonary inflammatory response to particles, Ann. Occup. Hyg., 46, 242-245, https://doi.org/10.1093/annhyg/mef684, 2002.

Eeftens, M., Meier, R., Schindler, C., Aguilera, I., Phuleria, H., Ineichen, A., Davey, M., Ducret-Stich, R., Keidel, D., Probst-Hensch, N., Kunzli, N., and Tsai, M. Y.: Development of land use regression models for nitrogen dioxide, ultrafine particles, lung deposited surface area, and four other markers of particulate matter pollution in the Swiss SAPALDIA regions, Environ. Health, 15, 53, https://doi.org/10.1186/s12940-016-0137-9, 2016.

Faraway, J. J.: Linear models with R, CRC press, 2014.

Fernández-Guisuraga, J. M., Castro, A., Alves, C., Calvo, A., Alonso-Blanco, E., Blanco-Alegre, C., Rocha, A., and Fraile, R.: Nitrogen oxides and ozone in Portugal: trends and ozone estimation in an urban and a rural site, Environ. Sci. Pollut. R., 23, 17171-17182, https://doi.org/10.1007/s11356-016-6888-6, 2016.

Fissan, H., Neumann, S., Trampe, A., Pui, D., and Shin, W.: Rationale and principle of an instrument measuring lung deposited nanoparticle surface area, J. Nanopart. Res., 53-59, https://doi.org/10.1007/s11051-006-9156-8, 2006.

Fung, P. L., Zaidan, M. A., Sillanpaa, S., Kousa, A., Niemi, J. V., Timonen, H., Kuula, J., Saukko, E., Luoma, K., Petaja, T., Tarkoma, S., Kulmala, M., and Hussein, T.: Input-Adaptive Proxy for Black Carbon as a Virtual Sensor, Sensors (Basel), 20, https://doi.org/10.3390/s20010182, 2020.

Fung, P. L., Zaidan, M. A., Surakhi, O., Tarkoma, S., Petäjä, T., and Hussein, T.: Data imputation in in situ-measured particle size distributions by means of neural networks, Atmos. Meas. Tech., 14, 5535–5554, https://doi.org/10.5194/amt-14-5535-2021, 2021a.

Fung, P. L., Zaidan, M. A., Timonen, H., Niemi, J. V., Kousa, A., Kuula, J., Luoma, K., Tarkoma, S., Petäjä, T., Kulmala, M., and Hussein, T.: Evaluation of white-box versus black-box machine learning models in estimating ambient black carbon concentration, J. Aerosol Sci., https://doi.org/10.1016/j.jaerosci.2020.105694, 2021b.

Gramsch, E., Reyes, F., Oyola, P., Rubio, M., López, G., Pérez, P., and Martínez, R.: Particle size distribution and its relationship to black carbon in two urban and one rural site in Santiago de Chile, J. Air Waste Manag. Assoc., 64, 785-796, https://doi.org/10.1080/10962247.2014.890141, 2014.

Gupta, R., and Xie, H.: Nanoparticles in daily life: applications, toxicity and regulations, J. Environ. Pathol. Tox., 37, https://doi.org/10.1615/JEnvironPatholToxicolOncol.2018026009, 2018.

Habre, R., Zhou, H., Eckel, S. P., Enebish, T., Fruin, S., Bastain, T., Rappaport, E., and Gilliland, F.: Short-term effects of airport-associated ultrafine particle exposure on lung function and inflammation in adults with asthma, Environ. Int., 118, 48-59, https://doi.org/10.1016/j.envint.2018.05.031, 2018.

Hagler, G. S. W., Williams, R., Papapostolou, V., and Polidori, A.: Air Quality Sensors and Data Adjustment Algorithms: When Is It No Longer a Measurement?, Environ. Sci. Technol., 52, 5530-5531, https://pubs.acs.org/doi/10.1021/acs.est.8b01826, 2018.

Hama, S. M. L., Ma, N., Cordell, R. L., Kos, G. P. A., Wiedensohler, A., and Monks, P. S.: Lung deposited surface area in Leicester urban background site/UK: Sources and contribution of new particle formation, Atmos. Envrion., 151, 94-107, https://doi.org/10.1016/j.atmosenv.2016.12.002, 2017.

Hastie, T., Tibshirani, R., and Tibshirani, R.: Best Subset, Forward Stepwise or Lasso? Analysis and Recommendations Based on Extensive Comparisons, Stat. Sci., 35, 579-592, https://doi.org/10.1214/19-STS733, 2020.

Helin, A., Niemi, J. V., Virkkula, A., Pirjola, L., Teinilä, K., Backman, J., Aurela, M., Saarikoski, S., Rönkkö, T., Asmi, E., and Timonen, H.: Characteristics and source apportionment of black carbon in the Helsinki metropolitan area, Finland, Atmos. Envrion., 190, 87-98, https://doi.org/10.1016/j.atmosenv.2018.07.022, 2018.

Hellén, H., Kangas, L., Kousa, A., Vestenius, M., Teinilä, K., Karppinen, A., Kukkonen, J., and Niemi, J. V.: Evaluation of the impact of wood combustion on benzo [a] pyrene (BaP) concentrations; ambient measurements and dispersion modeling in Helsinki, Finland, Atmos. Chem. Phys., 17, 3475-3487, https://doi.org/10.5194/acp-17-3475-2017, 2017.

Hennig, F., Quass, U., Hellack, B., Kupper, M., Kuhlbusch, T. A. J., Stafoggia, M., and Hoffmann, B.: Ultrafine and Fine Particle Number and Surface Area Concentrations and Daily Cause-Specific Mortality in the Ruhr Area, Germany, 2009-2014, Environ. Health Persp., 126, 027008, https://doi.org/10.1289/EHP2054, 2018.

Hinds, W. C.: Aerosol technology: properties, behavior, and measurement of airborne particles, John Wiley & Sons, 1999.

Hofmann, W.: Modelling particle deposition in human lungs: modelling concepts and comparison with experimental data, Biomarkers, 14, 59-62, https://doi.org/10.1080/13547500902965120, 2009.

ICRP: PUBLICATION 66: Human Respiratory Tract Model for Radiological Protection, Pergamon Press, New York, 1994.

Jafar, H. A., and Harrison, R. M.: Spatial and temporal trends in carbonaceous aerosols in the United Kingdom, Atmos. Pollut. Res., 12, 295-305, https://doi.org/10.1016/j.apr.2020.09.009, 2021.

Järvi, L., Hannuniemi, H., Hussein, T., Junninen, H., Aalto, P. P., Hillamo, R., Mäkelä, T., Keronen, P., Siivola, E., and Vesala, T.: The urban measurement station SMEAR III: Continuous monitoring of air pollution and surface–atmosphere interactions in Helsinki, Finland, Boreal Environ. Res., 19, 86-109, 2009.

Järvinen, A., Kuuluvainen, H., Niemi, J. V., Saari, S., Dal Maso, M., Pirjola, L., Hillamo, R., Janka, K., Keskinen, J., and Rönkkö, T.: Monitoring urban air quality with a diffusion charger based electrical particle sensor, Urban Clim., 14, 441-456, https://doi.org/10.1016/j.uclim.2014.10.002, 2015.

Järvinen, A., Timonen, H., Karjalainen, P., Bloss, M., Simonen, P., Saarikoski, S., Kuuluvainen, H., Kalliokoski, J., Dal Maso, M., Niemi, J. V., Keskinen, J., and Rönkkö, T.: Particle emissions of Euro VI, EEV and retrofitted EEV city buses in real traffic, Environ. Pollut., 250, 708-716, https://doi.org/10.1016/j.envpol.2019.04.033, 2019.

Johansson, L., Epitropou, V., Karatzas, K., Karppinen, A., Wanner, L., Vrochidis, S., Bassoukos, A., Kukkonen, J., and Kompatsiaris, I.: Fusion of meteorological and air quality data extracted from the web for personalized environmental information services, Environ. Modell. Softw., 64, 143-155, https://doi.org/10.1016/j.envsoft.2014.11.021, 2015.

Karjalainen, P., Timonen, H., Saukko, E., Kuuluvainen, H., Saarikoski, S., Aakko-Saksa, P., Murtonen, T., Bloss, M., Maso, M. D., Simonen, P., Ahlberg, E., Svenningsson, B., Brune, W. H., Hillamo, R., Keskinen, J., and Rönkkö, T.: Time-resolved characterization of primary particle emissions and secondary particle formation from a modern gasoline passenger car, Atmos. Chem. Phys., 16, 8559-8570, https://doi.org/10.5194/acp-16-8559-2016, 2016.

Kiriya, M., Okuda, T., Yamazaki, H., Hatoya, K., Kaneyasu, N., Uno, I., Nishita, C., Hara, K., Hayashi, M., Funato, K., Inoue, K., Yamamoto, S., Yoshino, A., and Takami, A.: Monthly and Diurnal Variation of the Concentrations of Aerosol Surface Area in Fukuoka, Japan, Measured by Diffusion Charging Method, Atmosphere (Basel), 8, https://doi.org/10.3390/atmos8070114, 2017.

Kulkarni, P., Baron, P. A., and Willeke, K.: Aerosol measurement: principles, techniques, and applications, John Wiley & Sons, 2011.

Kuula, J., Kuuluvainen, H., Rönkkö, T., Niemi, J. V., Saukko, E., Portin, H., Aurela, M., Saarikoski, S., Rostedt, A., Hillamo, R., and Timonen, H.: Applicability of Optical and Diffusion Charging-Based Particulate Matter Sensors to Urban Air Quality Measurements, Aerosol Air Qual. Res., 19, 1024-1039, https://doi.org/10.4209/aaqr.2018.04.0143, 2019.

Kuula, J., Kuuluvainen, H., Niemi, J. V., Saukko, E., Portin, H., Kousa, A., Aurela, M., Rönkkö, T., and Timonen, H.: Long-term sensor measurements of lung deposited surface area of particulate matter emitted from local vehicular and residential wood combustion sources, Aerosol Sci. Tech., 54, 190-202, https://doi.org/10.1080/02786826.2019.1668909, 2020.

Kuuluvainen, H., Rönkkö, T., Järvinen, A., Saari, S., Karjalainen, P., Lähde, T., Pirjola, L., Niemi, J. V., Hillamo, R., and Keskinen, J.: Lung deposited surface area size distributions of particulate matter in different urban areas, Atmos. Envrion., 136, 105-113, https://doi.org/10.1016/j.atmosenv.2016.04.019, 2016.

Kuuluvainen, H., Poikkimaki, M., Jarvinen, A., Kuula, J., Irjala, M., Dal Maso, M., Keskinen, J., Timonen, H., Niemi, J. V., and Ronkko, T.: Vertical profiles of lung deposited surface area concentration of particulate matter measured with a drone in a street canyon, Environ. Pollut., 241, 96-105, https://doi.org/10.1016/j.envpol.2018.04.100, 2018.

Lamberg, H., Nuutinen, K., Tissari, J., Ruusunen, J., Yli-Pirilä, P., Sippula, O., Tapanainen, M., Jalava, P., Makkonen, U., Teinilä, K., Saarnio, K., Hillamo, R., Hirvonen, M.-R., and Jokiniemi, J.: Physicochemical characterization of fine particles from small-scale wood combustion, Atmos. Envrion., 45, 7635-7643, https://doi.org/10.1016/j.atmosenv.2011.02.072, 2011.

Lindstrom, M. J., and Bates, D. M.: Newton—Raphson and EM algorithms for linear mixed-effects models for repeated-measures data, J. Am. Stat. Assoc., 83, 1014-1022, https://doi.org/10.2307/2290128, 1988.

Liu, H., Zhang, X., Zhang, H., Yao, X., Zhou, M., Wang, J., He, Z., Zhang, H., Lou, L., Mao, W., Zheng, P., and Hu, B.: Effect of air pollution on the total bacteria and pathogenic bacteria in different sizes of particulate matter, Environ. Pollut., 233, 483-493, https://doi.org/10.1016/j.envpol.2017.10.070, 2018a.

Liu, Y., Wu, J., Yu, D., and Hao, R.: Understanding the patterns and drivers of air pollution on multiple time scales: the case of northern China, Environ. Manage., 61, 1048-1061, https://doi.org/10.1007/s00267-018-1026-5, 2018b.

Luoma, K., Niemi, J. V., Aurela, M., Fung, P. L., Helin, A., Hussein, T., Kangas, L., Kousa, A., Rönkkö, T., Timonen, H., Virkkula, A., and Petäjä, T.: Spatiotemporal variation and trends in equivalent black carbon in the Helsinki metropolitan area in Finland, Atmos. Chem. Phys., 21, 1173-1189, https://doi.org/10.5194/acp-21-1173-2021, 2021.

Maricq, M. M.: Monitoring Motor Vehicle PM Emissions: An Evaluation of Three Portable Low-Cost Aerosol Instruments, Aerosol Sci. Tech., 47, 564-573, https://doi.org/10.1080/02786826.2013.773394, 2013.

Mikkonen, S., Németh, Z., Varga, V., Weidinger, T., Leinonen, V., Yli-Juuti, T., and Salma, I.: Decennial time trends and diurnal patterns of particle number concentrations in a central European city between 2008 and 2018, Atmos. Chem. Phys., 20, 12247-12263, https://doi.org/10.5194/acp-20-12247-2020, 2020.

Miller, A.: Subset selection in regression, CRC Press, 2002.

NCRP: Report No. 125: Deposition, Retention and Dosimetry of Inhaled Radioactive Substances, National Council on Radiation Protection and Measurements, 1997.

Oberdorster, G.: Nanotoxicology: in vitro-in vivo dosimetry, Environ. Health Persp., 120, A13; author reply A13, https://doi.org/10.1289/ehp.1104320, 2012.

Oberdörster, G., Maynard, A., Donaldson, K., Castranova, V., Fitzpatrick, J., Ausman, K., Carter, J., Karn, B., Kreyling, W., Lai, D., Olin, S., Monteiro-Riviere, N., Warheit, D., Yang, H., and A report from the ILSI Research Foundation/Risk Science

Institute Nanomaterial Toxicity Screening Working Group: Principles for characterizing the potential human health effects from exposure to nanomaterials: elements of a screening strategy, Part. Fibre Toxicol., 2, 1-35, https://doi.org/10.1186/1743-8977-2-8, 2005.

Pacitto, A., Stabile, L., Russo, S., and Buonanno, G.: Exposure to Submicron Particles and Estimation of the Dose Received by Children in School and Non-School Environments, Atmosphere (Basel), 11, https://doi.org/10.3390/atmos11050485, 2020.

Petäjä, T., Kerminen, V.-M., Maso, M. D., Junninen, H., Koponen, I., Hussein, T., Aalto, P. P., Andronopoulos, S., Robin, D., Hämeri, K., Bartzis, J. G., and Kulmala, M.: Sub-micron atmospheric aerosols in the surroundings of Marseille and Athens: physical characterization and new particle formation, Atmos. Chem. Phys., 7, 2705-2720, https://doi.org/10.5194/acp-7-2705-2007, 2007.

Pirjola, L., Niemi, J. V., Saarikoski, S., Aurela, M., Enroth, J., Carbone, S., Saarnio, K., Kuuluvainen, H., Kousa, A., Rönkkö, T., and Hillamo, R.: Physical and chemical characterization of urban winter-time aerosols by mobile measurements in Helsinki, Finland, Atmos. Environ., 158, 60-75, https://doi.org/10.1016/j.atmosenv.2017.03.028, 2017.

Reche, C., Viana, M., Brines, M., Perez, N., Beddows, D., Alastuey, A., and Querol, X.: Determinants of aerosol lung-deposited surface area variation in an urban environment, Sci. Total Environ., 517, 38-47, https://doi.org/10.1016/j.scitotenv.2015.02.049, 2015.

Rolph, G., Stein, A., and Stunder, B.: Real-time Environmental Applications and Display sYstem: READY, Environ. Model. Softw., 95, 210-228, https://doi.org/10.1016/j.envsoft.2017.06.025, 2017.

Rönkkö, T., Kuuluvainen, H., Karjalainen, P., Keskinen, J., Hillamo, R., Niemi, J. V., Pirjola, L., Timonen, H. J., Saarikoski, S., Saukko, E., Järvinen, A., Silvennoinen, H., Rostedt, A., Olin, M., Yli-Ojanperä, J., Nousiainen, P., Kousa, A., and Dal Maso, M.: Traffic is a major source of atmospheric nanocluster aerosol, Proc. Natl. Acad. Sci. U.S.A., 114, 7549-7554, https://doi.org/10.1073/pnas.1700830114, 2017.

Rostedt, A., Arffman, A., Janka, K., Yli-Ojanperä, J., and Keskinen, J.: Characterization and Response Model of the PPS-M Aerosol Sensor, Aerosol Sci. Tech., 48, 1022-1030, https://doi.org/10.1080/02786826.2014.951023, 2014.

Rudin, C.: Stop explaining black box machine learning models for high stakes decisions and use interpretable models instead, Nat. Mach. Intell., 1, 206-215, https://doi.org/10.1038/s42256-019-0048-x, 2019.

Salo, L., Hyvärinen, A., Jalava, P., Teinilä, K., Hooda, R. K., Datta, A., Saarikoski, S., Lintusaari, H., Lepistö, T., Martikainen, S., Rostedt, A., Sharma, V. P., Rahman, M. H., Subudhi, S., Asmi, E., Niemi, J. V., Lihavainen, H., Lal, B., Keskinen, J., Kuuluvainen, H., Timonen, H., and Rönkkö, T.: The characteristics and size of lung-depositing particles vary significantly between high and low pollution traffic environments, Atmos. Environ., 118421, https://doi.org/10.1016/j.atmosenv.2021.118421, 2021a.

Salo, L., Rönkkö, T., Saarikoski, S., Teinilä, K., Kuula, J., Alanen, J., Arffman, A., Timonen, H., and Keskinen, J.: Concentrations and Size Distributions of Particle Lung-deposited Surface Area (LDSA) in an Underground Mine, Aerosol Air Qual. Res., 21, 200660-200660, https://doi.org/10.4209/aaqr.200660, 2021b.

Schmid, O., and Stoeger, T.: Surface area is the biologically most effective dose metric for acute nanoparticle toxicity in the lung, J. Aerosol Sci., 99, 133-143, https://doi.org/10.1016/j.jaerosci.2015.12.006, 2016.

Shiraiwa, M., Ueda, K., Pozzer, A., Lammel, G., Kampf, C. J., Fushimi, A., Enami, S., Arangio, A. M., Fröhlich-Nowoisky, J., Fujitani, Y., Furuyama, A., Lakey, P. S. J., Lelieveld, J., Lucas, K., Morino, Y., Pöschl, U., Takahama, S., Takami, A., Tong, H., Weber, B., Yoshino, A., and Sato, K.: Aerosol health effects from molecular to global scales, Environ. Sci. Technol., 51, 13545-13567, https://doi.org/10.1021/acs.est.7b04417, 2017.

Šimić, I., Lovrić, M., Godec, R., Kröll, M., and Bešlić, I.: Applying machine learning methods to better understand, model and estimate mass concentrations of traffic-related pollutants at a typical street canyon, Environ. Pollut., 263, 114587, https://doi.org/10.1016/j.envpol.2020.114587, 2020.

Taylor, K. E.: Summarizing multiple aspects of model performance in a single diagram, J. Geophys. Res. Atmos., 106, 7183-7192, https://doi.org/10.1029/2000JD900719, 2001.

Teinilä, K., Aurela, M., Niemi, J. V., Kousa, A., Petäjä, T., Järvi, L., Hillamo, R., Kangas, L., Saarikoski, S., and Timonen, H.: Concentration variation of gaseous and particulate pollutants in the Helsinki city centre—Observations from a two-year campaign from 2013–2015, Boreal Environ. Res., 2019.

Timonen, H., Carbone, S., Aurela, M., Saarnio, K., Saarikoski, S., Ng, N. L., Canagaratna, M. R., Kulmala, M., Kerminen, V.-M., Worsnop, D. R., and Hillamo, R.: Characteristics, sources and water-solubility of ambient submicron organic aerosol in springtime in Helsinki, Finland, J. Aerosol Sci., 56, 61-77, https://doi.org/10.1016/j.jaerosci.2012.06.005, 2013.

Tissari, J.: Fine particle emissions from residential wood combustion (Puun pienpolton pienhiukkaspäästöt), University of Kuopio, Finland, 63 pp., 2008.

Todea, A. M., Beckmann, S., Kaminski, H., and Asbach, C.: Accuracy of electrical aerosol sensors measuring lung deposited surface area concentrations, J. Aerosol Sci., 89, 96-109, https://doi.org/10.1016/j.jaerosci.2015.07.003, 2015.

Tong, X., Ho, J. M. W., Li, Z., Lui, K.-H., Kwok, T. C., Tsoi, K. K., and Ho, K.: Prediction model for air particulate matter levels in the households of elderly individuals in Hong Kong, Sci. Total Environ., 717, 135323, https://doi.org/10.1016/j.scitotenv.2019.135323, 2020.

Yeh, H.-C., and Schum, G.: Models of human lung airways and their application to inhaled particle deposition, B. Math. Biol., 42, 461-480, https://doi.org/10.1016/S0092-8240(80)80060-7, 1980.

Zaidan, M. A., Wraith, D., Boor, B. E., and Hussein, T.: Bayesian proxy modelling for estimating black carbon concentrations using white-box and black-box models, Appl. Sci., 9, 4976, https://doi.org/10.3390/app9224976, 2019.

Zaidan, M. A., Motlagh, N. H., Fung, P. L., Lu, D., Timonen, H., Kuula, J., Niemi, J. V., Tarkoma, S., Petäjä, T., Kulmala, M., and Hussein, T.: Intelligent calibration and virtual sensing for integrated low-cost air quality sensors, IEEE Sens. J., 20, 13638-13652, 2020.

751 Zhou, Y., Dada, L., Liu, Y., Fu, Y., Kangasluoma, J., Chan, T., Yan, C., Chu, B., Daellenbach, K. R., Bianchi, F., Kokkonen,
752 T. V., Liu, Y., Kujansuu, J., Kerminen, V.-M., Petäjä, T., Wang, L., Jiang, J., and Kulmala, M.: Variation of size-segregated
753 particle number concentrations in wintertime Beijing, Atmos. Chem. Phys., 20, 1201-1216, https://doi.org/10.5194/acp-20-
754 1201-2020, 2020.

755

756 **Table 1.** Ambient LDSA of alveolar region (in µm^2 cm^{-3}, corrected to 2 significant figures) reported in the last decade in chronological
757 order of the measurement start. TS and RA represent traffic sites and residential area respectively. For the other acronyms, please see the
758 method section.

Site description	Location	Average (Mean, unless state otherwise)	Uncertainties (SD, unless state otherwise)	Period/Season	Instruments	Study
UB	Ruhr, Germany	median=36	IQR=21	Mar 2009–Dec 2014	NSAM	Hennig et al. (2018)
RB+UB+TS	Basel, Geneva, Lugano, Wald, Switerland	32	IQR=25	Jan 2011–Dec 2012	DiSCmini	Eeftens et al. (2016)
City centre with heavy traffic	Lisbon, Portugal	35–89	4–8	Apr–May 2011	NSAM	Albuquerque et al. (2012)
UB	Cassino, Italy	88–240	-	Oct 2011– Mar 2012	NSAM	Buonanno et al. (2012)
RB		69				
UB with traffic influence	Barcelona, Spain	37	26	Nov 2011–May 2013	NSAM	Reche et al. (2015)
TS	Helsinki, Finland	65–94	-	Feb 2012	ELPI, NSAM	Kuuluvainen et al. (2016)
RA		15–31				
TS	Athens, Greece	65	21 4.8	Jul 2012	Partector Aerotrak 9000	Cheristanidis et al. (2020)
UB with traffic influence	Leichester, UK	30	25	Nov 2013–May 2015	NSAM	Hama et al. (2017)
		23	14	Warm months		
		38	33	Cold months		
Airport	Los Angeles	47	27	Nov–Dec 2014 and May–Jul 2015	DiSCmini	Habre et al. (2018)
UB	Fukuoka, Japan	127	62	Apr 2015–Mar 2016	NSAM	Kiriya et al. (2017)
TS	Helsinki, Finland	60 (ground level) 36-40 (below rooftop) 16-26 (above rooftop)		Nov 2016	Partector, ELPI, DiSCmini,	Kuuluvainen et al. (2018)

					Pegasor AQ Urban	
SC	Helsinki, Finland	22	14	Feb 2017–Jan 2018	Pegasor AQ Urban	Kuula et al. (2020)
UB		9.4	6.9			
DH		12	10			
TS	Delhi, India	330	130	Nov–Dec 2018	ELPI	Salo et al. (2021a)
UB	Salerno	79	48	Nov 2018–May 2019	NanoTracer	Pacitto et al. (2020)
TS	Roma, Italy	110	57			
RB	Parma, Italy	17	10			

759

760

761

762 **Table 2.** Descriptive statistics of alveolar LDSA concentrations (μm^2 cm^{-3}) at SC (2017–2018), UB (2017–May 2018), DH1–3 (2018) and
763 RB (2018) site. The mean (column 3), standard deviation (SD, column 4), 10th, 25th, 50th, 75th and 90th percentile (P10, P25, P50, P75 and
764 P90, column 5–9), geometric mean (Gmean, column 10) and geometric standard deviation (GSD, column 11) of the concentrations are
765 corrected to one decimal place. The percentage of valid data in the reported measurement period is shown in column 12.

		Mean	SD	P10	P25	P50	P75	P90	Gmean	GSD	%
SC	All	19.7	11.3	8.4	11.7	17.0	24.7	34.4	17.0	1.7	97
	Winter	19.4	12.2	7.6	10.7	16.1	24.7	35.3	16.3	1.8	98
	Spring	19.6	11.0	8.6	11.8	16.9	24.3	34.2	17.1	1.7	94
	Summer	20.8	10.4	10.5	13.5	18.4	25.5	34.2	18.6	1.6	98
	Autumn	18.4	11.7	7.1	10.0	15.0	23.8	34.6	15.3	1.8	96
	Workdays	21.4	12.3	8.6	12.5	18.8	27.7	37.6	18.4	1.8	97
	Weekends	15.9	7.5	8.1	10.7	14.4	19.4	25.2	14.4	1.6	97
UB	All	11.2	7.1	4.6	6.4	9.5	14.0	19.6	9.5	1.8	70
	Winter	12.4	9.1	4.8	6.3	10.0	15.4	22.5	10.1	1.9	89
	Spring	10.4	6.1	4.6	6.2	9.0	12.8	18.3	9.0	1.7	100
	Summer	12.8	5.8	6.7	8.5	11.4	15.8	20.7	11.6	1.6	57
	Autumn	7.7	4.7	3.2	4.5	6.7	9.7	13.2	6.7	1.7	56
	Workdays	11.5	7.3	4.8	6.7	9.7	14.1	20.3	9.8	1.8	70
	Weekends	10.4	6.6	4.1	5.8	8.8	13.6	18.3	8.8	1.8	70
DH1–3	All	11.7	8.6	4.2	6.3	9.7	14.5	21.1	9.5	1.9	94
	Winter	12.3	10.2	4.1	6.2	9.6	14.8	23.4	9.7	2.0	86
	Spring	12.8	8.2	5.3	7.4	10.8	15.9	23.1	10.7	1.8	98
	Summer	11.8	5.9	5.7	7.8	10.8	14.5	19.2	10.6	1.6	98
	Autumn	10.5	10.2	3.0	4.6	6.8	13.0	22.2	7.5	2.2	95
	Workdays	11.8	8.3	4.3	6.4	9.9	14.6	20.8	9.6	1.9	95
	Weekends	11.7	9.3	4.0	6.0	9.4	14.3	21.8	9.3	2.0	93
RB	All	7.6	5.4	2.4	4.0	6.5	10.2	14.0	6.1	2.0	99
	Winter	6.6	6.0	2.2	3.5	5.6	8.3	11.6	5.3	1.9	100
	Spring	9.1	6.4	3.5	5.1	7.4	11.0	16.6	7.5	1.9	99
	Summer	9.8	4.3	4.7	6.6	9.3	12.5	15.3	8.9	1.6	99
	Autumn	4.9	4.1	1.6	2.6	3.9	5.6	8.9	3.8	2.0	99
	Workdays	7.7	5.6	2.5	4.1	6.6	10.2	14.1	6.2	2.0	99
	Weekends	7.6	5.0	2.4	4.0	6.5	10.1	14.0	6.1	2.0	100

766

767

768

769 **Table 3.** The evaluation attributes by IAME model at the SC and the UB site, corrected to 2 significant figures.

	Street canyon					Urban background				
	R^2	MAE	$cRMSD$	r	NSD	R^2	MAE	$cRMSD$	r	NSD
All	0.80	3.7	5.6	0.87	0.78	0.77	2.3	3.7	0.86	0.80
Winter	0.86	3.4	5.3	0.92	0.74	0.81	2.5	4.6	0.89	0.68
Spring	0.75	3.9	5.9	0.85	0.79	0.61	2.4	3.3	0.84	0.85
Summer	0.70	4.1	5.9	0.83	0.84	0.61	2.7	3.7	0.79	0.95
Autumn	0.85	3.4	5.4	0.9	0.75	0.85	1.3	2.0	0.91	0.83
Workdays	0.81	4.1	6.1	0.87	0.77	0.75	2.4	3.8	0.86	0.77
Weekends	0.72	3.0	4.3	0.82	0.82	0.8	2.1	3.5	0.85	0.87

770

771

772 **Table 4.** Five most successful sub-models at the SC site. The table shows only the fixed predictors with their coefficient (β, all p<0.05) and
773 corresponding standard error (SE). The variance inflation factor (VIF) among the fixed predictors is also shown for the 5 sub-models. The
774 evaluation attributes of the sub-models are shown column 6–10. The percentage of the sub-model usage and the number of data points (n)
775 is shown in column 11 and 12. Natural logarithm is taken for parameters with asterisk (*).

	Fixed predictors	β	SE	VIF	R^2	MAE	cRMSD	r	NSD	%	n
	*$PM_{2.5}$	0.119	0.005	1.54							
1	*PNC	0.313	0.005	2.89	0.74	3.7	5.7	0.87	0.79	81	2603
	*BC	0.223	0.004	2.17							
	*NOx	0.236	0.005	3.79							
2	*PNC	0.153	0.005	1.63	0.74	3.8	5.7	0.86	0.77	13	2629
	*BC	0.231	0.007	4.90							
	*PNC	−0.044	0.003	1.07							
3	*BC	0.375	0.004	2.20	0.74	3.8	5.8	0.86	0.78	4	6622
	WS	0.201	0.004	2.15							
	*NO_x	0.250	0.005	3.09							
4	*$PM_{2.5}$	0.243	0.004	1.17	0.74	3.8	5.7	0.87	0.78	<1	2596
	*PNC	0.184	0.005	3.02							
	*NOx	0.176	0.005	3.51							
5	*PM_{10}	0.070	0.004	1.3	0.72	3.8	5.8	0.85	0.75	<1	2713
	*BC	0.326	0.006	3.65							

776
777

778 **Table 5.** Five most successful sub-models at the UB site. The table shows only the fixed predictors with their coefficient (β, all $p<0.05$) and
779 corresponding standard error (SE). The variance inflation factor (VIF) among the fixed predictors is also shown for the 5 sub-models. The
780 evaluation attributes of the sub-models are shown column 6–10, corrected to 2 significant figures. The percentage of the sub-model usage
781 and the number of data points (n) is shown in column 11 and 12. Natural logarithm is taken for parameters with asterisk (*).

	Fixed predictors	β	SE	VIF	R^2	MAE	cRMSD	r	NSD	%	n
	*CO	0.072	0.027	1.72							
1	*PNC	0.400	0.006	2.08	0.84	1.7	2.5	0.92	0.87	49	941
	*BC	2.956	0.007	1.52							
	*PNC	−0.098	0.005	1.09							
2	*BC	0.398	0.004	1.44	0.82	1.9	2.9	0.91	0.89	17	6608
	WD-N	0.328	0.006	1.55							
	*NO$_2$	0.237	0.007	1.88							
3	*CO	0.520	0.024	1.10	0.69	2.4	3.4	0.84	0.73	17	941
	*PNC	0.341	0.010	2.00							
	*CO	0.009	0.000	1.08							
4	*PNC	0.348	0.025	1.07	0.58	2.7	3.9	0.77	0.63	11	9757
	RH	0.590	0.007	1.15							
	*NO$_x$	0.107	0.006	2.22							
5	*CO	0.182	0.032	1.72	0.81	1.9	3.0	0.90	0.85	2	7036
	*BC	0.455	0.007	2.56							

782
783
784
785

786 **Table 6.** Model evaluation comparison of deposition model derived LDSA (LDSA$_{ICRP}$), modelled LDSA by IAP (LDSA$_{IAP}$) and modelled
787 LDSA by IAME (LDSA$_{IAME}$) against reference measurements LDSA$_{Pegasor}$ at the SC and the UB site. Parameters with an asterisk represent
788 natural logarithm. The evaluation attributes of the three methods are corrected to 2 significant figures.

	Street canyon					Urban background				
	R^2	MAE	$cRMSD$	r	NSD	R^2	MAE	$cRMSD$	r	NSD
LDSA$_{ICRP}$	0.72	4.1	6.2	0.88	1.1	0.83	1.8	2.9	0.93	1.1
LDSA$_{IAP}$	0.77	4.0	6.0	0.85	0.78	0.66	2.8	3.9	0.84	0.81
LDSA$_{IAME}$	0.80	3.7	5.6	0.87	0.78	0.77	2.3	3.7	0.86	0.80

789

790

	Street canyon					Urban background				
	R^2	MAE	$cRMSD$	r			R^2	MAE	$cRMSD$	r	NSD

791 **Table 7.** Statistics to show temporal difference. The number of data (n), mean and standard deviation (SD) of absolute error and the
792 corresponding p-values of t-tests at the selected time windows at both sites.

Street canyon (SC)	n	Mean	SD	t-test	p
Workdays	11658	4.1	4.8	Workdays vs Weekends	4.13×10^{-81}
Weekends	5322	3.0	3.2		
				Winter vs Spring	3.64×10^{-24}
Winter	4023	3.4	4.2	Winter vs Summer	5.89×10^{-5}
Spring	2297	4.0	4.5	Winter vs Autumn	7.07×10^{-7}
Summer	6457	4.2	4.4	Spring vs Summer	6.38×10^{-34}
Autumn	4320	3.4	4.3	Spring vs Autumn	1.02×10^{-4}
				Summer vs Autumn	2.69×10^{-15}
Hour 4–10 a.m.	4953	4.8	5.6	Hour 4–10 a.m. vs	2.58×10^{-40}
Hour 4–10 p.m.	4981	3.5	3.6	4–10 p.m.	

793

Urban background (UB)	n	Mean	SD	t-test	p
Workdays	8473	2.3	2.6	Workdays vs Weekends	5.08×10^{-8}
Weekends	3852	2.1	2.6		
				Winter vs Spring	1.96×10^{-7}
Winter	2539	2.5	3.2	Winter vs Summer	0.39***
Spring	1101	1.9	3.1	Winter vs Autumn	1.90×10^{-2}
Summer	1628	2.6	2.4	Spring vs Summer	2.75×10^{-9}
Autumn	812	2.3	2.1	Spring vs Autumn	2.20×10^{-3}
				Summer vs Autumn	1.40×10^{-3}
Hour 4–10 a.m.	3620	2.3	2.7	Hour 4–10 a.m. vs	0.86***
Hour 4–10 p.m.	3591	2.3	2.7	4–10 p.m.	

794

	n	Mean	SD	t-test	p
Street canyon (SC)	11940	3.9	4.6	SC vs UB	8.21×10^{-246}
Urban background (UB)		2.3	2.6	(in same time period)	

795 *** $p > 0.05$ the null hypothesis of different distribution is rejected

796

797
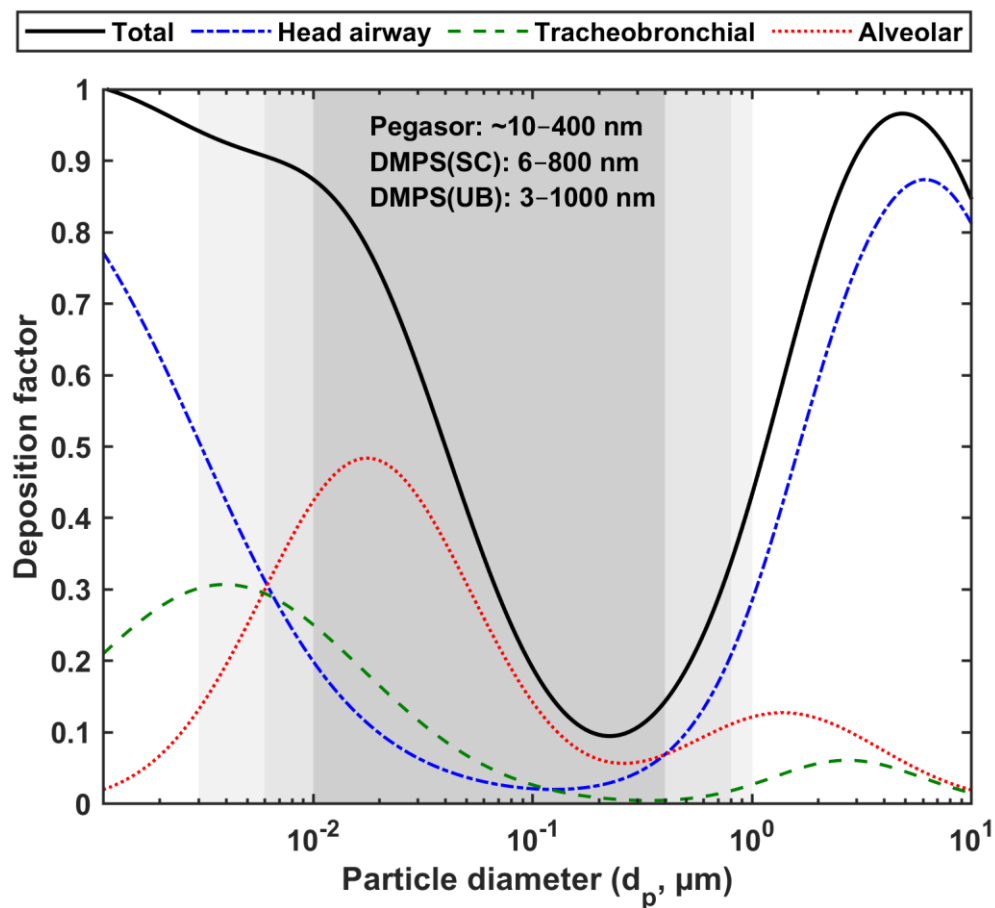
Figure 1. Lung deposition factor of a spectrum of particle size distribution based on the equation (ICRP, 1994). Black solid line represents the total deposition factor while blue, green and red dotted line refer to deposition factor in head airway, tracheobronchial and alveolar region, respectively. Pegasor AQ Urban measured the alveolar LDSA concentration of particles in the ~10–400 nm size range (dark grey). DMPS at SC and UB were used to calculate alveolar LDSA in selected size fractions in the 6–800 nm and 3–1000 nm size range, respectively.

798
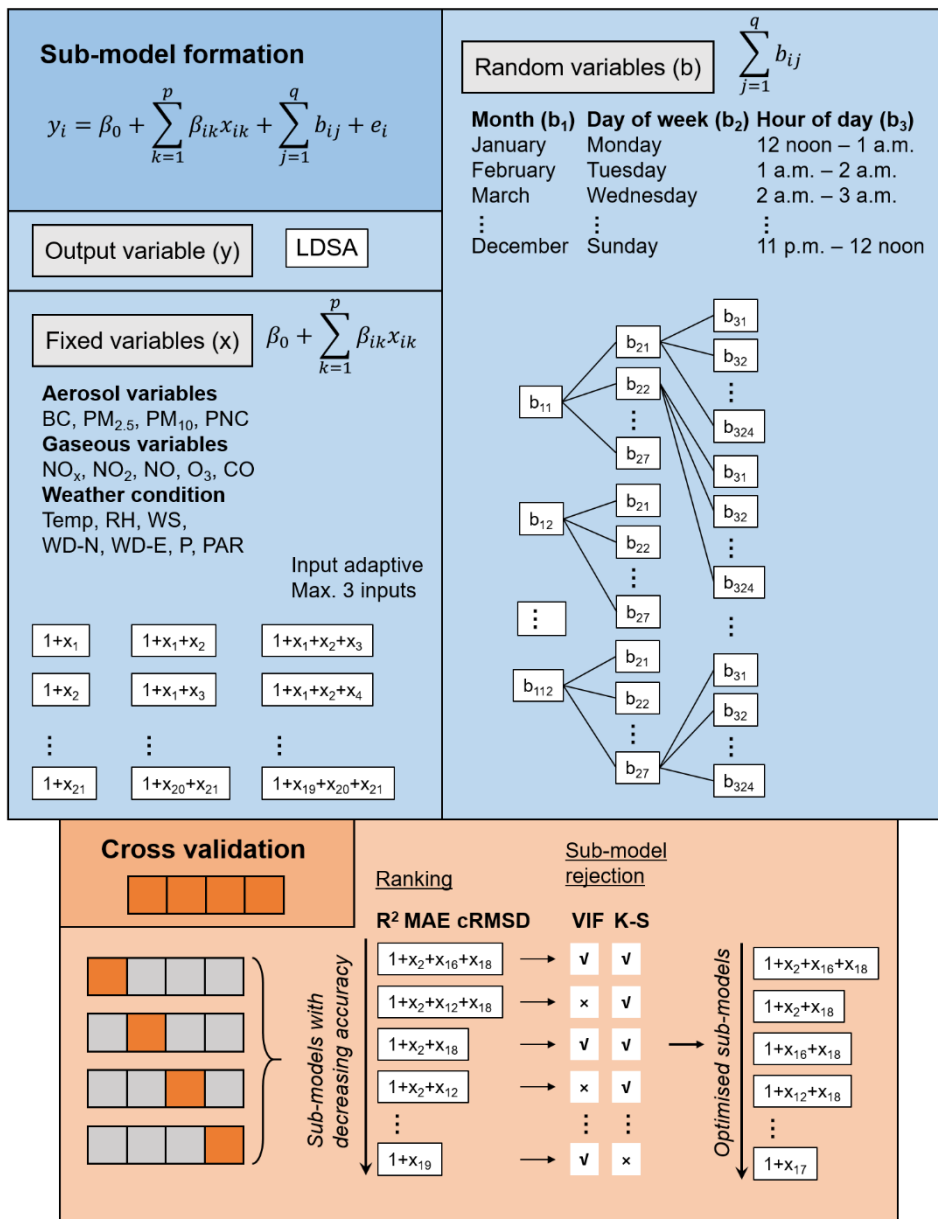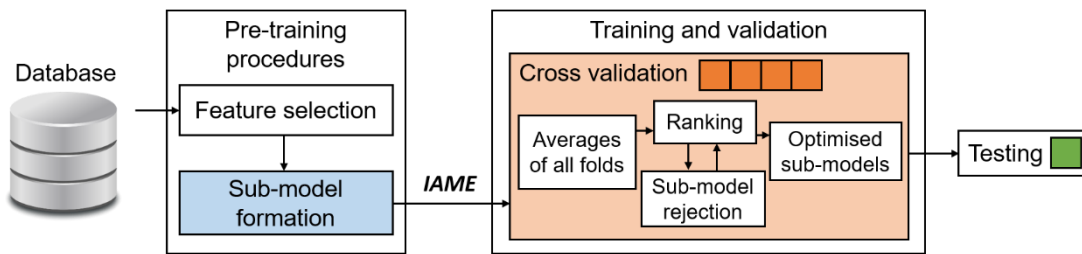
Figure 2. The block diagram of the proxy procedures (top). The blue and orange blocks are explanatory notes to the sections of sub-model formation and cross validation, respectively.

799
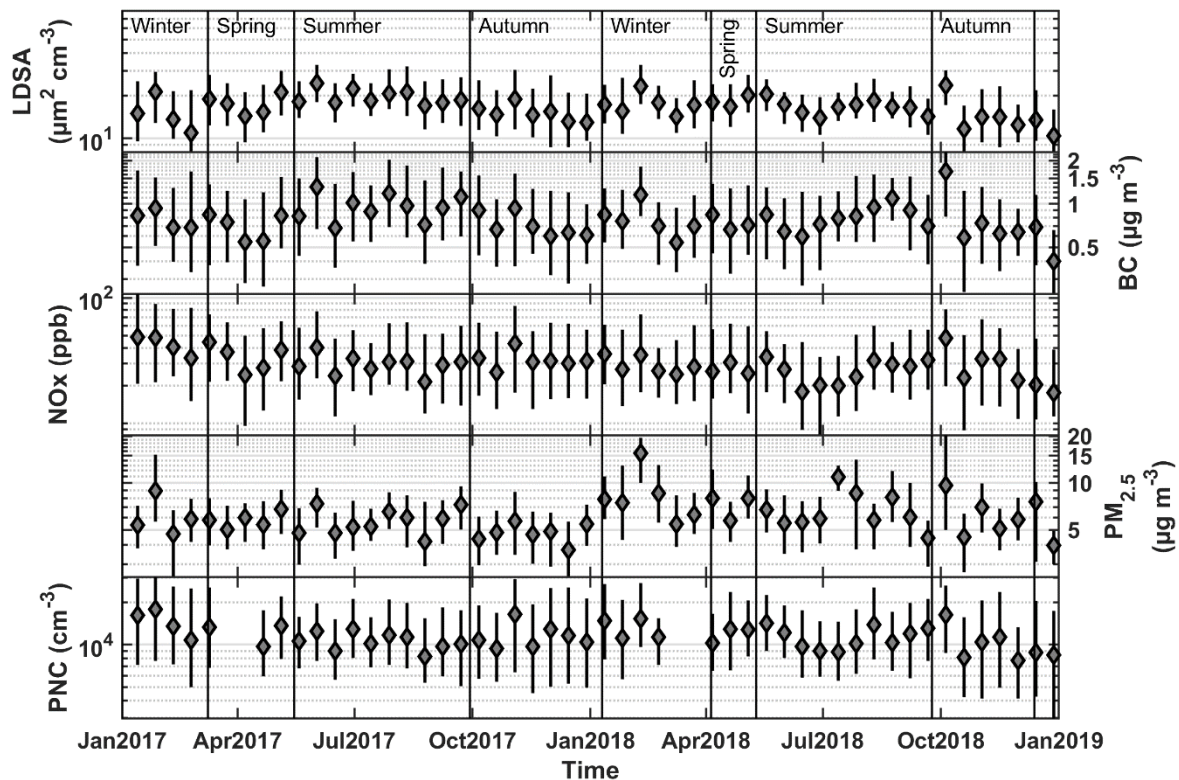
Figure 3. Time series of the selected air pollutant parameters (First to end row: LDSA (μm^2 cm^{-3}), BC (μg m^{-3}), NO_x (ppb), $PM_{2.5}$ (μg m^{-3}) and PNC (cm^{-3})) at Mäkelänkatu SC site during the measurement period from 1 January 2017 and 31 December 2018. Each bar represents a period of two weeks where the shaded diamond marker is the median and the vertical error bars are the 25th and 75th percentiles. Seasons are thermally separated.

800

801

802
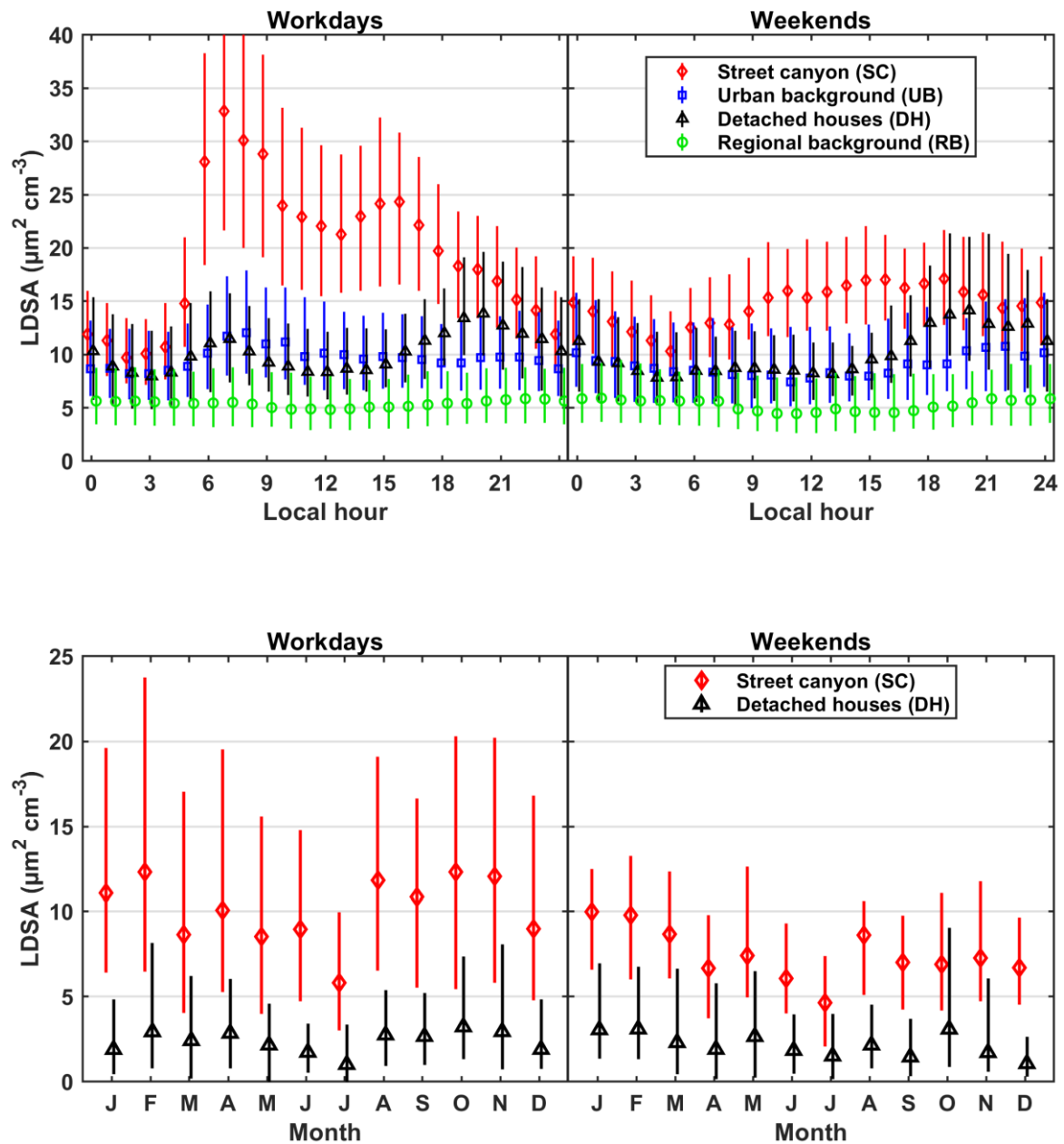
Figure 4. Upper panel: Diurnal cycles of LDSA concentrations ($\mu m^2 \ cm^{-3}$) at SC (red diamond, 2017–2018), UB (blue square, 2017–May 2018), DH1–3 (black triangle, 2018) and RB site (green circle, 2018) on workdays and weekends with error bars of 25th and 75th percentiles. Lower panel: Monthly averages in year 2018 of local LDSA increments at the SC (red diamond) and DH1–3 (black triangle) site (LDSA concentration at the hotspot site – LDSA at RB site) on workdays and weekends with error bars of 25th and 75th percentiles.

803

804
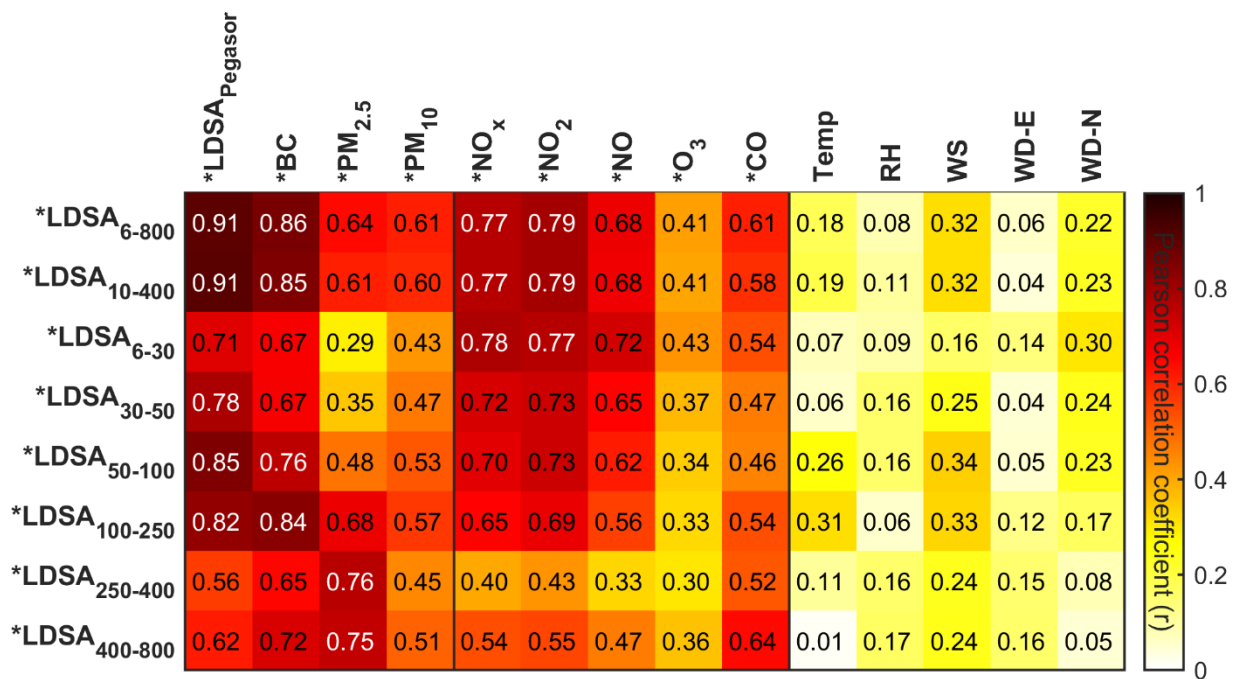
Figure 5. Heatmap showing Pearson correlation coefficient (r, corrected to 2 significant figures) of LDSA of different particle size sections (in nm) by ICRP lung deposition model and the other air pollutant parameters at Mäkelänkatu SC site. Dark red indicates a high correlation while pale yellow indicates a low correlation. Parameters with an asterisk represent natural logarithm. $LDSA_{Pegasor}$ represents the measured LDSA concentrations.

805
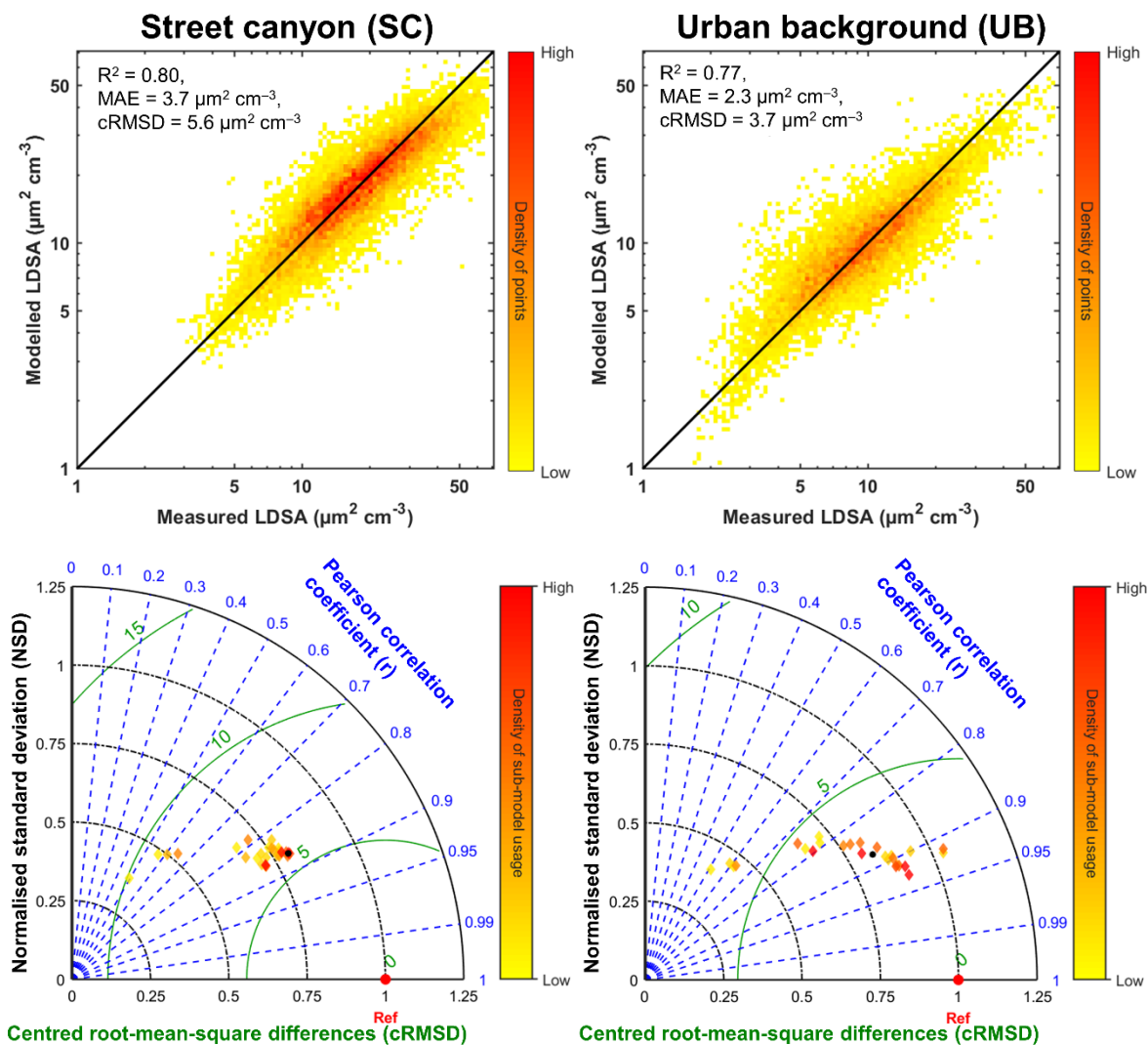
Figure 6. The upper panel shows the scatter plots of modelled LDSA against the measured LDSA at Mäkelänkatu SC site (first column) and at Kumpula UB site (second column). Hues of colours represent the density of points on the figure. The lower panel shows the Taylor's diagrams (Taylor, 2001) at Mäkelänkatu SC site (first column) and at Kumpula UB site (second column). Each diamond marker in the Taylor's diagrams represents each sub-model used in the final estimation by IAME (solid black dot), compared with the reference data (solid red dot). Hues of colours represent how frequent the sub-model was used.

806

807
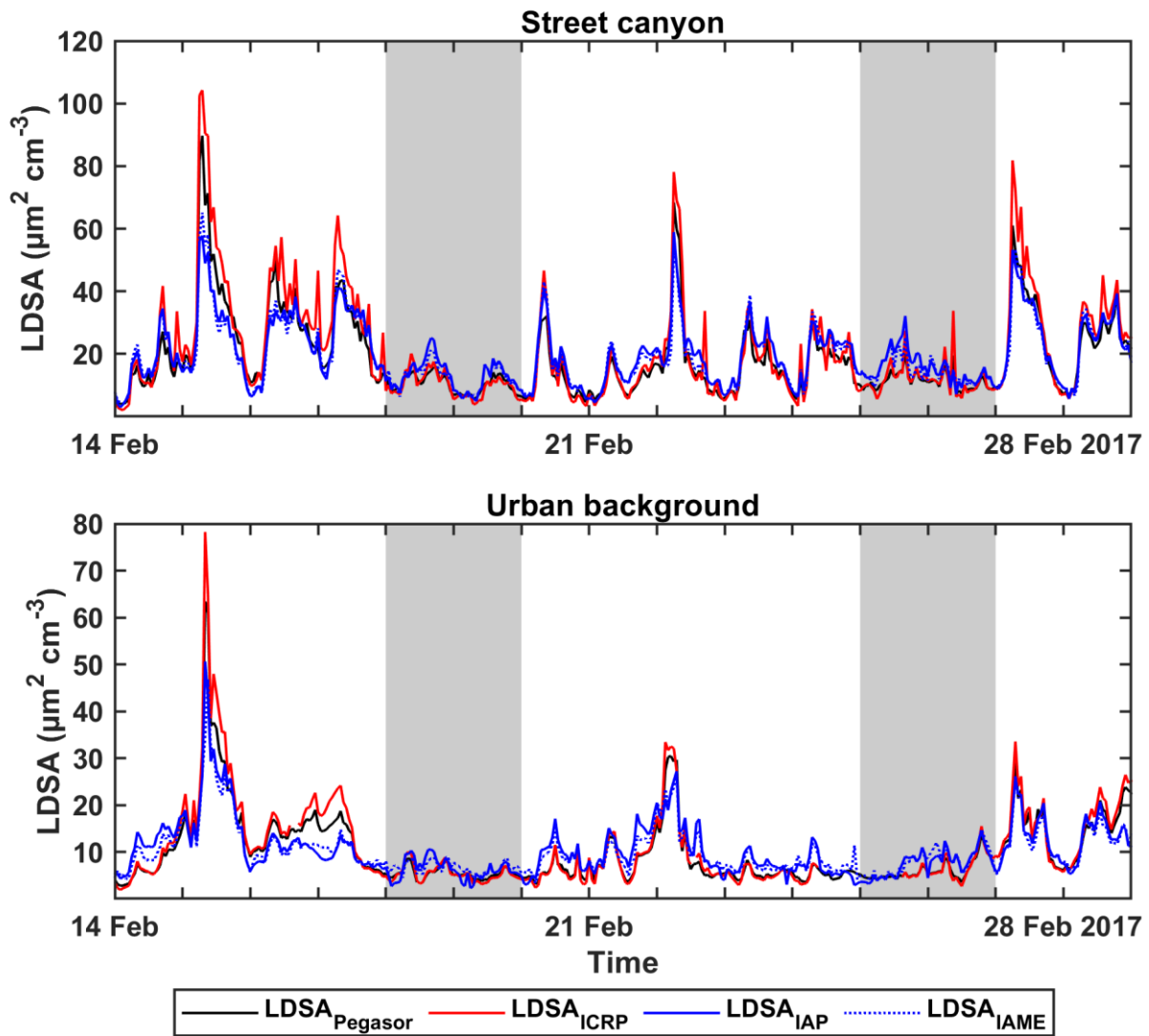
Figure 7. Timeseries of measured LDSA (LDSA_Pegasor, black), deposition model derived LDSA by ICRP (LDSA_ICRP, red), modelled LDSA by IAP (LDSA_IAP, blue solid line) and modelled LDSA by IAME (LDSA_IAME, blue dotted line) during a selected measurement window between 14 and 28 February 2017. Shaded regions represent weekends, otherwise workdays.

808

809
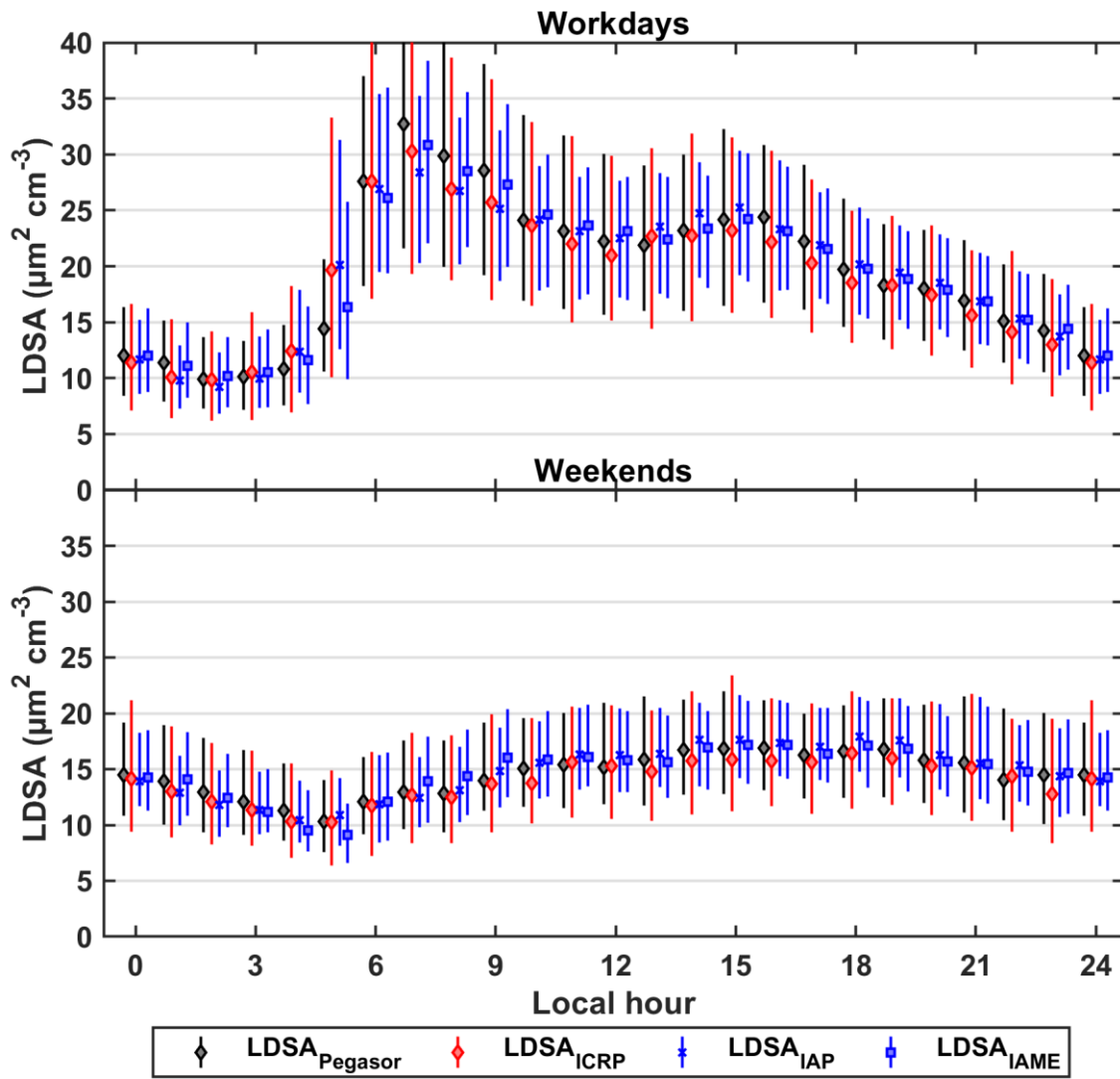
Figure 8. Diurnal cycles of measured (LDSA_Pegasor, black), deposition model derived (LDSA_ICRP, red) and modelled (LDSA_IAP and LDSA_IAME, blue) LDSA concentrations with error bars of 25th and 75th percentiles on workdays (left) and weekends (right). LDSA_IAP and LDSA_IAME can be differentiated by their markers, cross for the former and square for the latter.

810

811